Backbone curves of coupled cubic oscillators in one-to-one internal resonance: bifurcation scenario, measurements and parameter identification

Arthur Givois · Jin-Jack Tan · Cyril Touzé · Olivier Thomas

Abstract A system composed of two cubic nonlinear oscillators with close natural frequencies, and thus displaying a 1:1 internal resonance, is studied both theoretically and experimentally, with a special emphasis on the free oscillations and the backbone curves. The instability regions of uncoupled solutions are derived and the bifurcation scenario as a function of the parameters of the problem is established, showing in an exhaustive manner all possible solutions. The backbone curves are then experimentally measured on a circular plate, where the asymmetric modes are known to display companion configurations with close eigenfrequencies. A control system based on a Phase-Locked Loop (PLL) is used to measure the backbone curves and also the frequency response function in the forced and damped case, including unstable branches. The model is used for a complete identification of the unknown parameters and an excellent comparison is drawn out between theoretical prediction and measurements.

Keywords Nonlinear vibrations · Backbone curve · Bifurcations · 1:1 Resonance · Stability · Measurements · Model identification

A. Givois (✉) · O. Thomas
Arts et Metiers Institute of Technology, LISPEN, HESAM Université, F-59000 Lille, France
e-mail: arthur.givois@ensam.eu

A. Givois
Conservatoire National des Arts et Métiers, LMSSC EA 3196, 292 rue Saint-Martin, 75141 Paris Cedex 03, France

J.-J. Tan · C. Touzé
IMSIA, CNRS, CEA, ENSTA Paris, Institut Polytechnique de Paris, 828 Boulevard des Maréchaux, 91762 Palaiseau Cedex, France

J.-J. Tan
Eindhoven University of Technology, PO Box 513, 5600 MB Eindhoven, The Netherlands

1 Introduction

Nonlinear system displaying internal resonance has been the subject of a number of studies as a strong nonlinear coupling could lead to solutions that are completely different from linear predictions [4, 12, 24, 25, 27, 40, 42]. Internal resonance is closely related to the normal form theory and Poincaré's theorem where the specific resonance relationship between eigenfrequencies is linked to a resonant monom that cannot be cancelled through a near-identity transform [15, 31, 44, 46]. In vibration theory, these systems are usually denoted in series of numbers, e.g. 1:2 and 1:1:2, which refers to the relationship between the eigenfrequencies of the system. For instance, a 1:2 resonant system has eigenfrequencies related by $\omega_2 \simeq 2\omega_1$ while a 1:1:2 system exhibits $\omega_2 \simeq \omega_1$ and $\omega_3 \simeq 2\omega_1$.

Among all possible internal resonances, 1:1 resonance is described by two oscillators having close eigenfrequencies and may appear as the simplest one and the first to be studied. It occurs in numerous mechanical systems having known symmetries such as strings, where the two polarizations of a same mode have close eigenfrequencies [13, 14, 37, 38]; beams [1, 26]; and two-dimensional structures with obvious symmetry such as circular plates [32, 39, 45, 47] square membranes or plates [6, 9, 48], or circular cylindrical shells [44]. The resonant monoms related to 1:1 resonance are of cubic order so that quadratic nonlinearity is of no concern in this case. In most of these studies, the emphasis is put on deriving the forced vibration response, and less studies are directly concerned with the the freely vibrating 1:1 internal resonance scenario.

Restricting attention to the free vibration, the papers by Lewandowski in the early 90s give the first contributions to understand the bifurcation points found on backbone curves. Analytical results obtained on the case of a beam with 1:3 internal resonance were first derived [19], and then extended to plates and membranes featuring either 1:1 or 1:3 internal resonance [20]. The analytical methods used a two-mode approximation and a single-harmonic component in the time domain. A seminal study on the 1:1 internal resonance has been provided by Manevitch and Manevitch [21]. In particular, they derive the possible solutions for cubic oscillators deriving from a potential, thus restricting to three parameters for describing the nonlinear coupling coefficients. They also provide a complete study of the possible cases with varying parameters, expressing the solutions in terms of first integral of motions and ratio of amplitudes obtained after numerous changes of coordinates, rendering the solutions sometimes difficult to read. More recently, the bifurcation of the backbones in case of 1:1 resonance has also been studied in [5], but with restriction to a single case of coefficients values, thus not bringing important novel results as compared to the exhaustive study by Manevitch and Manevitch.

Meanwhile, advances of dedicated experimental continuation methods allows easier and more reliable measurements of backbone curves as well as unstable branches of forced and damped systems. Among them, the control-based techniques that are founded on a path-following approach of an arclength parameter and stabilized via feedback control, have managed to obtain backbone curves and bifurcations experimentally for single degree-of-freedom nonlinear systems [3, 33, 36]. An alternative approach where control of the phase is achieved via a phase-locked loop (PLL) procedure has lead to the measurement of frequency response functions of a piezoelectric ring in high-amplitude nonlinear regimes [22]. Denis et al. has further shown that the PLL technique allows measurement of the frequency responses on both sides of the phase resonances including the unstable part [7]. Despite the requirement of a monotonous evolution of the phase, the robustness and efficiency of the PLL control are demonstrated in the aforementioned piezoelectric systems [7, 22], in musical instruments like Chinese gongs [16] and also in the current work.

For unforced conservative systems, there is an equivalence between the backbone curves of a nonlinear system and its nonlinear modes, since a backbone represents the frequency dependence on amplitude, when ones spans the family of periodic orbits (or the equivalent invariant manifold) [34, 35]. In this framework, internal resonance is usually identified as loops in the backbone curve, as shown for example in [17], with the peculiar feature that the internal resonance occurs on the nonlinear frequencies, far from their linear values. In the present case of a 1:1 internal resonance between the linear eigenfrequencies, the topology of the backbone curves is found to show more cases than only simple loops, with no unique qualitative topology, giving new insights in the behaviour of nonlinear modes. Another important aspect is the experimental identification of nonlinear modes, which has been a very active subject during the recent years (see, for instance, [7, 28]). Since most of the techniques rely on complex identification algorithms which aims at extending the ones for linear systems widely used in industrial contexts [29], we propose here a simple identification method based on the available model, following the unimodal technique introduced in [7].

In the present contribution, a theoretical investigation of the bifurcation scenario for the backbone curves of a system displaying 1:1 internal resonance is detailed, followed by measurements on a circular plate. As compared to previous studies, the main outcomes are to generalize the results obtained in [21] to four nonlinear coupling parameters. More importantly, instability regions for uncoupled solutions are derived, a point that were not present in [5, 20, 21], and

is important, since it gives a more direct and simpler analysis of the bifurcation scenario. These instability regions are found by comparison with the forced and damped cases. The theoretical analyses are all presented in Sect. 2. Then, an experimental procedure based on the PLL control is applied to measure the first asymmetric modes of a freely vibrating circular plate. The backbone curves and bifurcation scenarios of such a 1:1 internal resonance system are identified. These are all presented in Sect. 3, which also includes descriptions of the experimental procedures and the estimation of the nonlinear coefficients. Finally, the paper is concluded in Sect. 4.

2 Theoretical results

The theoretical derivations are devoted to expressing the backbone curves for a system of two cubic nonlinear oscillators with close eigenfrequencies. Denoting X_1 and X_2 the displacements of oscillator 1 and 2, the equations of motion under study read:

$$\ddot{X}_1 + \omega_1^2 X_1 + \varepsilon\left[\Gamma_1 X_1^3 + C_1 X_1 X_2^2\right] = 0, \tag{1a}$$

$$\ddot{X}_2 + \omega_2^2 X_2 + \varepsilon\left[\Gamma_2 X_2^3 + C_2 X_2 X_1^2\right] = 0, \tag{1b}$$

where ε is a book-keeping parameter, ω_1 and ω_2 are the two eigenfrequencies such that $\omega_1 \simeq \omega_2$, Γ_1 and Γ_2 are the leading cubic coefficients for each oscillator, and C_1 and C_2 are the cross-coupling coefficients. The choice of this formulation is guided by the following considerations:

- In a normal form approach [44, 46], one can show that quadratic nonlinearity does not lead to resonant terms for the 1:1 internal resonance when $\omega_1 \simeq \omega_2$. Consequently there is no need to take them into account.
- The general normal form for a system with cubic nonlinearity should also include the monoms $X_1^2 X_2$ and X_2^3 for the first oscillator, and $X_2^2 X_1$ and X_1^3 for the second oscillator. Here we select a simplest form depending on four parameters only, Γ_1, Γ_2, C_1 and C_2 instead of the most general form including 8 coefficients. The reason is that for most of the mechanical systems like strings, beams and plates, the symmetry relationships leads to equations of the form (1). Consequently it has been decided to restrict our attention to a four-parameter problem with varying coefficients. This point will be further discussed in Sects. 3 and 4.

When $C_1 = C_2 = C$, the stiffness derives from the potential energy $\mathcal{V}$:

$$\mathcal{V} = \frac{1}{2}\left(\omega_1^2 X_1^2 + \omega_2^2 X_2^2\right) + \frac{\varepsilon}{4}\left(\Gamma_1 X_1^4 + 2C X_1^2 X_2^2 + \Gamma_2 X_2^4\right). \tag{2}$$

This case was considered by Manevitch and Manevitch in [21]. In order to extend their result to a more general case with four parameters and include the possibility of taking into account slight imperfections of real structures, we will also consider the case $C_1 \neq C_2$ in this study.

The solutions of this nonlinear problem is derived thanks to a first-order perturbative approach using the method of multiple time scales. As most of the derivations of the perturbative solution are classical, they are given in "Appendix 1", where a special emphasis is also put on deriving the first-order equations for both the forced/damped case and the free case, in order to show the similarity and differences occurring in the two sets of equations. In this section, only the main results are recalled, the reader is referred to "Appendix 1" for the detailed calculations.

A detuning σ_1 is introduced in order to quantify the difference between the two eigenfrequencies:

$$\omega_2 = \omega_1 + \varepsilon\sigma_1. \tag{3}$$

Without loss of generality, we can assume $\sigma_1 \geq 0$, which is not restrictive and only means that oscillator 2 is the one with the larger eigenfrequency. The two time scales $T_0 = t$ and $T_1 = \varepsilon t$ are introduced, and the solution is expressed under the form $X_i = X_{i1}(T_0, T_1) + \varepsilon X_{i2}(T_0, T_1)$, $i = 1, 2$. The first-order solution reads

$$X_{11} = A(T_1)\exp(i\omega_1 T_0) + c.c., \tag{4a}$$

$$X_{21} = B(T_1)\exp(i\omega_2 T_0) + c.c., \tag{4b}$$

where $c.c.$ stands for complex conjugate. Finally the unknown amplitudes $A(T_1)$ and $B(T_1)$ are expressed in polar form, $A = a(T_1)\exp(i\alpha(T_1))$, $B = b(T_1)\exp(i\beta(T_1))$. In order to make the slow-scale first-order system autonomous, the following change of variable is introduced for the angles:

$$\gamma_1 = -\alpha, \tag{5a}$$

$$\gamma_2 = -\sigma_1 T_1 - \beta. \tag{5b}$$

As explained in A, this choice is motivated by direct comparisons with the forced/damped system. Finally, the slow-scale autonomous system reads:

$$a' = -\frac{C_1}{2\omega_1} a b^2 \sin 2(\gamma_1 - \gamma_2), \tag{6a}$$

$$\gamma_1' = -\frac{3\Gamma_1}{2\omega_1} a^2 - \frac{C_1}{2\omega_1} b^2 [2 + \cos 2(\gamma_1 - \gamma_2)], \tag{6b}$$

$$b' = \frac{C_2}{2\omega_2} b a^2 \sin 2(\gamma_1 - \gamma_2), \tag{6c}$$

$$\gamma_2' = -\frac{3\Gamma_2}{2\omega_2} b^2 - \frac{C_2}{2\omega_2} a^2 [2 + \cos 2(\gamma_1 - \gamma_2)] - \sigma_1. \tag{6d}$$

The solutions of (6) are obtained after integration with respect to the slow time T_1. Two kinds of solutions exist:

- The uncoupled solutions, where a single mode is excited while the other stay quiescent. Two uncoupled solutions exist and will be denoted as the A-mode for which $a \neq 0$ and $b = 0$, and the B-mode, for which $b \neq 0$ and $a = 0$,
- The coupled solutions, for which both amplitude solutions are non zero, *i.e.* $a \neq 0$ and $b \neq 0$.

2.1 Uncoupled solutions and instability regions

The uncoupled solutions are easily derived from (6). They are defined by $a = \text{const}$, $b = 0$, $\gamma_1 = -3\Gamma_1/(2\omega_1) a^2 T_1 + \varphi_1$ and $b = \text{const}$, $a = 0$, $\gamma_2 = -(3\Gamma_2/(2\omega_2) b^2 + \sigma_1) T_1 + \varphi_2$, thus leading to:

$$\begin{aligned} X_1(t) &= 2a \cos\left(\omega_{NL}^A t - \varphi_1\right), \\ X_2(t) &= 2b \cos\left(\omega_{NL}^B t - \varphi_2\right), \end{aligned} \tag{7}$$

where φ_1 and φ_2 depend on the initial conditions. The associated backbone curves are:

for the A-mode:

$$\omega_{NL}^A = \omega_1 \left(1 + \varepsilon \frac{3\Gamma_1}{2\omega_1^2} a^2\right). \tag{8}$$

for the B-mode:

$$\omega_{NL}^B = \omega_2 \left(1 + \varepsilon \frac{3\Gamma_2}{2\omega_2^2} b^2\right). \tag{9}$$

where ω_{NL}^A (respectively ω_{NL}^B) refers to the nonlinear oscillation frequency of A-mode (resp. B-mode), as a function of its amplitude a (resp. b).

The next question to tackle is the derivation of the stability of these uncoupled solutions, in order to predict where a loss of stability can happen in favour of a coupled solution through activation of the 1:1 resonance. In previous works and particulary in the paper by Manevitch and Manevitch [21], instability regions were not derived, for the main reason that setting either $b = 0$ (to study the stability of the A-mode) or $a = 0$ (to study the stability of the B-mode) leads to a degenerate problem given by Eq. (6): the four-dimensional phase space shrinks to a two-dimensional one without any possibility of studying the stability with respect to vanishing directions. The solution is found by using the analysis of the system with forcing and damping, as shown in "Appendix 2". Then, taking the limit of vanishing damping and forcing, one is able to demonstrate (see "Appendix 2") that the stability region of the A-mode is bounded by the two following curves:

$$\omega_{Alim}^s = \omega_2 + \varepsilon(2 + s) \frac{C_2 a^2}{2\omega_2}, \quad \text{with } s = \pm 1. \tag{10}$$

Symmetrically, the instability region for the B-mode is bounded by the two curves:

$$\omega_{Blim}^s = \omega_1 + \varepsilon(2 + s) \frac{C_1 b^2}{2\omega_1}, \quad \text{with } s = \pm 1. \tag{11}$$

In particular, one can note that the stability of A-mode (resp. B-mode) is dictated by the value of the coupling coefficient C_2 (resp. C_1), which is logical since this term is responsible for the nonlinear energy transfer between the two oscillators.

The situation is illustrated in Fig. 1, which has been obtained for a perfect detuned case, *i.e.* with all nonlinear coefficients equal, here $\Gamma_1 = \Gamma_2 = C_1 = C_2 = 1$, and a detuning between the two eigenfrequencies with $\omega_1 = \pi$, $\varepsilon = 1$ and $\sigma_1 = 1$, thus leading to $\omega_2 = 1 + \pi$. Each instability region lies respectively in the plane of A-mode (*i.e.* where $b = 0$) and B-mode (where $a = 0$), and is delimited by two curves that are obtained by setting either $s = 1$ or $s = -1$. These two curves are plotted in red and green in Fig. 1. If the backbone curve of the

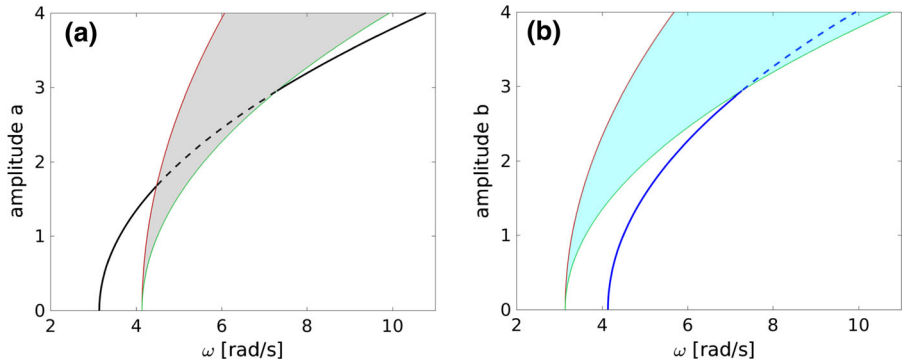

Fig. 1 Instability regions of the uncoupled solutions. **a** In the plane (ω, a), with $b = 0$ is the stability of the A-mode. The backbone curve given by Eq. (8) is in black (unstable part with dashed line), while the stability region delimited by Eqs. (10) is given by the thin red line (for $s = -1$) and green line (for $s = +1$). **b** In the plane (ω, b), with $a = 0$ is the stability of the B-mode. The backbone curve given by Eq. (9) is in blue (unstable part with dashed line), while the stability region delimited by Eqs. (10) is given by the thin red line (for $s = -1$) and green line (for $s = +1$). (Color figure online)

A-mode (resp. B-mode) enters the instability region delimited by the two curves given by Eqs. (10) and delimiting the grey-shaded area in Fig. 1a (resp. the blue-shaded areas in Fig. 1b), then the uncoupled solution becomes unstable. Note that the A-mode starts at ω_1 when $a \longrightarrow 0$, whereas the instability region starts at ω_2. Symmetrically, B-mode starts at ω_2 while the instability regions at ω_1. All curves are parabolas, and for the A-mode, the coefficient of the parabola is $\frac{3\Gamma_1}{2\omega_1}$, while the two instability curves are governed by $\frac{C_2}{2\omega_2}$ and $\frac{3C_2}{2\omega_2}$. Consequently one may also inspect the possible intersections of backbones with instability regions by simply looking at the nonlinear coefficients. In the case considered with $\Gamma_1 = \Gamma_2 = C_1 = C_2$, the A-mode crosses the instability region in two points, whereas the B-mode has only one crossing point with its instability region. This question will be further discussed when all possible solutions are described by varying the coefficients, see Sect. 2.3. It is a very important feature of this problem to understand that most of the topology of the solutions can be understood by simply looking at the coefficients values.

2.2 Coupled solutions and their stability

The coupled solutions have already been derived in [21] with the assumption $C_1 = C_2$, here we simply recall the main results. Inspection of non-zero constant solutions for the amplitudes a and b of the system (6) shows that uncoupled solutions can exist if and only if $\sin 2(\gamma_1 - \gamma_2) = 0$, which leads to the conclusion that we have necessarily $\cos 2(\gamma_1 - \gamma_2) = s = \pm 1$, where the notation $s = \pm 1$ is introduced for convenience. This choice leads to two different kind of solutions. If $s = +1$, then $\gamma_2 = \gamma_1 + p\pi$, with $p \in \mathbb{Z}$. Replacing this relationship in the phases α and β used in the polar form of the amplitudes $A(T_1)$ and $B(T_1)$, one can easily show that the solutions X_1 and X_2 fulfills the following relationship

$$\frac{X_1}{a} = \pm \frac{X_2}{b}, \tag{12}$$

with a positive case when p is even and a negative case when p is odd. Following Manevitch and Manevitch, this solution is called the *normal mode* (NM) and is represented in Fig. 2a. A normal mode is characterized by a phase difference of 0 (in-phase normal mode, for odd p) or π (out-of-phase normal mode for p even) between the two solutions, and in the configuration plane (X_1, X_2), the solutions are oscillating on a line as dictated by Eq. (12). In particular the two modes reach their maximum amplitudes at the same time.

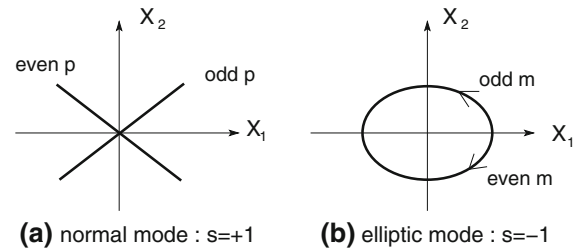

Fig. 2 Definition of normal mode and elliptic mode

The other case is obtained when $s=-1$, where $\gamma_2=\gamma_1+(2m+1)\frac{\pi}{2}$ for $m\in\mathbb{Z}$. One can easily show that the relationship between the amplitudes writes:

$$\frac{X_1^2}{4a^2}+\frac{X_2^2}{4b^2}=1, \tag{13}$$

These solutions are the *elliptic modes* (EM), as represented in Fig. 2b and are characterized by ellipses in the configuration space (X_1,X_2).

The solution branches for the coupled solutions are then simply obtained by remarking that with $s=\pm1$, $\gamma_1'=\gamma_2'$, which gives the following relationship:

$$\sigma_1=\left[\frac{3\Gamma_1}{2\omega_1}-(2+s)\frac{C_2}{2\omega_2}\right]a^2+\left[(2+s)\frac{C_1}{2\omega_1}-\frac{3\Gamma_2}{2\omega_2}\right]b^2, \tag{14}$$

with $s=+1$ for the normal mode solution and $s=-1$ for the elliptic mode solution. In order to represent this solution in the space spanned by the two amplitudes a, b, and the nonlinear oscillation frequency, one has to retrieve the backbone curve for the coupled solutions. Since the amplitudes a and b are constants with respect to T_1, integrating for example Eq. (6b) with respect to T_1 leads to

$$\gamma_1(T_1)=\left[-\frac{3\Gamma_1}{2\omega_1}a^2-(2+s)\frac{C_1b^2}{2\omega_1}\right]T_1+\varphi_1, \tag{15}$$

with φ_1 the initial phase corresponding to the initial conditions. Replacing in Eqs. (4a) and (4b) allows one to get the coupled solution:

$$\begin{aligned} X_1(t)&=2a\cos\left(\omega_{NL}^c t-\varphi_1\right),\\ X_2(t)&=\begin{cases}\pm2b\cos\left(\omega_{NL}^c t-\varphi_1\right), & \text{for } s=1\\ 2b\cos\left(\omega_{NL}^c t-\varphi_1\pm\pi/2\right), & \text{for } s=-1\end{cases}\end{aligned} \tag{16}$$

where the common nonlinear oscillation frequency ω_{NL}^c for the coupled solution is:

$$\omega_{NL}^c=\omega_1+\varepsilon\left[\frac{3\Gamma_1}{2\omega_1}a^2+(2+s)\frac{C_1b^2}{2\omega_1}\right], \tag{17}$$

with $s=+1$ for the normal mode, $s=-1$ for the elliptic mode, and a and b the amplitudes of the coupled solutions verifying Eq. (14).

The stability of the coupled solutions is found classically by computing the eigenvalues of the Jacobian matrix from the system (6), see "Appendix 3" for the detail of the calculation. One can then easily derive the following stability conditions for the coupled solutions, which extends the results by Manevitch and Manevitch [21] to the case $C_1\neq C_2$. The stability of both NM and EM depends only on the physical parameters of the system (*i.e.* eigenfrequencies and coupling coefficients), but not on the amplitudes of the solutions. Inded, the value of the scalar S_c is sufficient to decide upon the stability of coupled solutions, with S_c equals to

$$S_c=\frac{\Gamma_1\omega_2}{C_2\omega_1}+\frac{\Gamma_2\omega_1}{C_1\omega_2}. \tag{18}$$

The stability rules for the coupled solutions read

- The normal mode is stable as long as $S_c<2$,
- The elliptic mode is stable as long as $S_c>2/3$.

This very particular feature leads to the fact that the stability of the coupled solutions is pre-determined directly from the values of the parameters of the system.

Figure 3 shows the coupled solutions in the detuned perfect case studied before, *i.e.* for $\Gamma_1=\Gamma_2=C_1=C_2=1$, $\omega_1=\pi$, $\varepsilon=1$ and $\sigma_1=1$. As already noticed in Fig. 1, the A-mode has two intersections with the instability region, while the B-mode has only one intersection. From the first loss of stability of the backbone curve of the A-mode, an elliptic mode emerges. A supercritical pitchfork bifurcation occurs at this point, and the two bifurcated branches (coupled EM) have the same amplitude, so that only one curve appears in Fig. 3, but have a difference in the phase of the B-mode with respect to the A-mode, which is $\pm\pi/2$ as shown by Eq. (16). Indeed, the two EM with odd and even m resulting in a π difference between γ_1 and γ_2 branch from this point.

From the second intersection, a normal mode emerges and connects to the other branch point defined by the intersection of the backbone curve of the B-mode with the instability region. These two points thus define two subcritical pitchforks, where NM branches from the uncoupled solutions. Figure 3a shows a three-dimensional plot of the solutions in the space (ω,a,b), which is the correct representation to show the uncoupled solution, included respectively in the subplane (ω,a), and (ω,b), and the coupled solutions. Figure 3b, c shows the projections of the solutions on the planes (ω,a) and (ω,b).

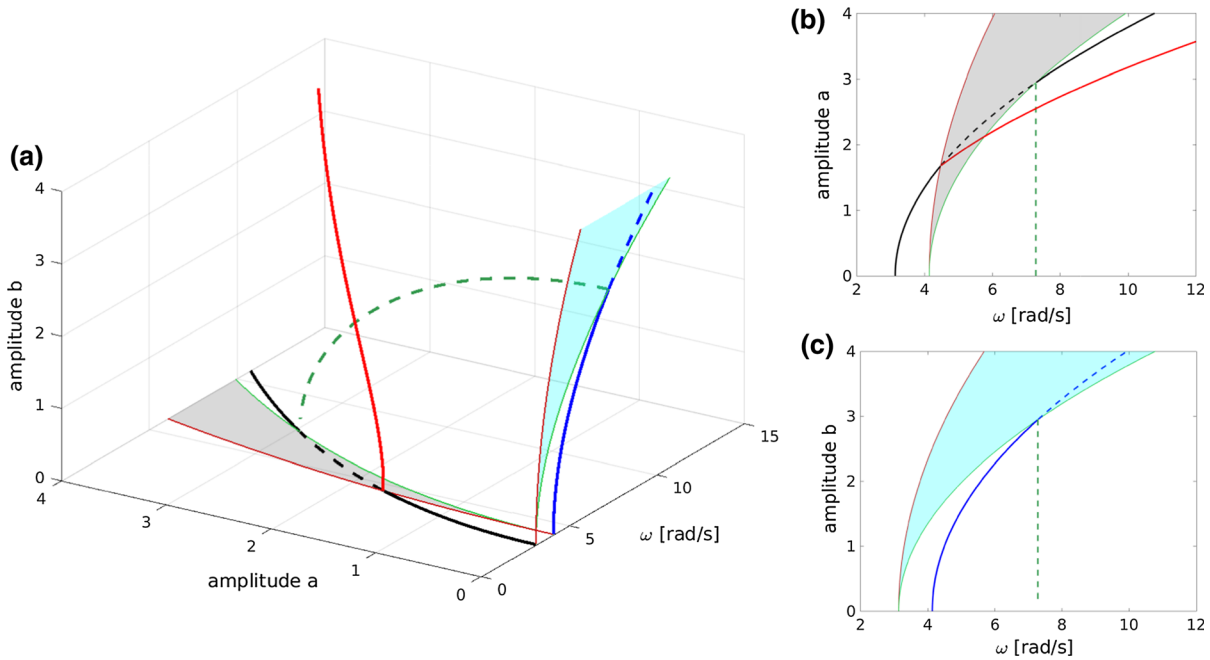

Fig. 3 **a** Three-dimensional representation of the solution branches in the (ω, a, b) space. Black line: backbone of the A-mode, blue line: backbone of the B-mode, red line: elliptic mode, green line: normal mode. Unstable solutions are marked as dashed lines, stable portions with solid lines. **b** Projection of the solutions in the (ω, a) plane. **c** Projection of the solutions in the (ω, b) plane. (Color figure online)

The stability of the coupled solutions is determined by the scalar S_c, which writes, for the particular perfect detuned case:

$$S_c = \frac{\omega_2 \Gamma_1}{C_2 \omega_1} + \frac{\Gamma_2 \omega_1}{C_1 \omega_2}, \tag{19}$$

$$= 1 + \varepsilon\sigma_1 + \frac{1}{1+\varepsilon\sigma_1}, \tag{20}$$

$$\simeq 2 + \varepsilon^2 \frac{\sigma_1^2}{2}. \tag{21}$$

The result has been obtained by simplification thanks to the equality between the coupling coefficients, and using $\omega_2 = \omega_1 + \varepsilon\sigma_1$. We can then simply deduce that the normal mode is unstable, while the elliptic mode is stable in this case, an information that is reported in Fig. 3.

2.3 Parametric study: bifurcation scenario

We are now interested in deriving all the possible cases when $\sigma_1 > 0$ and the nonlinear coupling coefficients are varying. In order to restrict a little the possible cases, we concentrate on a hardening type system with Γ_1, Γ_2, C_1, $C_2 > 0$. Note however that other cases with negative coefficients can easily be deduced from the present study. The particular case without detuning is derived in "Appendix 4": although this very specific case is hardly ever encoutered in real life applications, it presents some mathematical interests and completes the derivations of the present section.

As understood from the example shown in "Appendix 4", the backbone curves of the A-mode and the B-mode may have, depending on the relative values of the coefficients, either zero, one, or at most two intersections with the instability regions. These cases delimit the discussion and span the 9 possible cases.

Let us denote I_{Ea} as the intersection of the backbone curve of A-mode with the first instability region, and I_{Na} the intersection with the second curve. The situation is depicted in Fig. 4a. The points I_{Ea} and I_{Na} are thus found by equating Eq. (8) with Eq. (10) (with $s = \pm 1$) thus leading to:

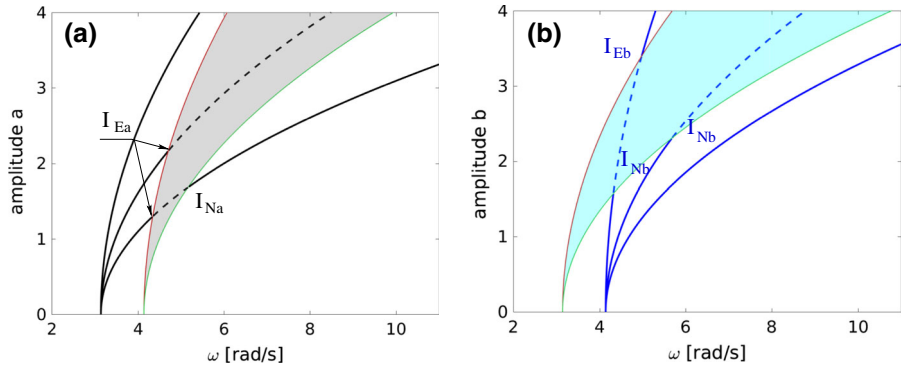

Fig. 4 **a** Definition of I_{Ea} and I_{Na} as intersection of the backbone curve of the A-mode with the two instability curves. Backbone curves for three different values of Γ_1: 0.3, 0.7 and 1.5, showing respectively no intersection, one intersection (only I_{Ea} exists) and two intersections. **b** Definition of I_{Eb} and I_{Nb} as intersection of the backbone curve of the B-mode with the two instability curves. Backbone curves for three different values of Γ_2: 0.2, 0.8 and 1.5, showing respectively two intersections, one intersection (only I_{Nb} exists) and no intersection. Other parameters are fixed as $C_1 = C_2 = 1$, $\omega_1 = \pi$, $\varepsilon = 1$ and $\sigma_1 = 1$. (Color figure online)

$$a^2 = \frac{\sigma_1}{\dfrac{3\Gamma_1}{2\omega_1} - (2+s)\dfrac{C_2}{2\omega_2}}, \tag{22}$$

with $s = -1$ for I_{Ea} and $s = +1$ for I_{Na}. Eq. (22) can also be retrieved from Eq. (14) by letting $b = 0$. The consequence of this is that I_{Ea} is a branch point where only an elliptic mode can branch with $s = -1$ (thus the index Ea as "Elliptic" mode from A-mode), and I_{Na} is a branch point to a normal mode.

The same reasoning on the B-mode leads to the conclusion that I_{Eb} and I_{Nb} are branch points leading respectively to elliptic mode and normal mode from the B-solution, and they are defined by:

$$b^2 = \frac{\sigma_1}{(2+s)\dfrac{C_1}{2\omega_1} - \dfrac{3\Gamma_2}{2\omega_2}}, \tag{23}$$

The main consequence is that EM can branch only from the left-hand side curve of the instability region, which has been thus reported in red in Figs. 1 and 3, it is also the colour retained to draw the backbone of the EM. On the other hand, NM can only branch from right-hand side curve from instability region, which is thus reported in green.

From Eqs. (22) and (23) we can easily derive existence conditions for the branch points, which read:

- I_{Ea} exists if $3\Gamma_1\omega_2 \geq C_2\omega_1$
- I_{Na} exists if $\Gamma_1\omega_2 \geq C_2\omega_1$
- I_{Eb} exists if $C_1\omega_2 \geq 3\Gamma_2\omega_1$
- I_{Nb} exists if $C_1\omega_2 \geq \Gamma_2\omega_1$.

Note that these conditions can also be found easily from the inspection of Fig. 4 by comparing the coefficients of the parabolas of each curve.

The 9 possible cases are represented in Fig. 5, where, for the sake of simplicity, Γ_1 and Γ_2 have been considered as fixed, and C_1 and C_2 as variable. The existence conditions of the branch points have been reported on the horizontal and vertical axes. For example when referring to C_1: no branch point exists when $C_1 < \Gamma_2\omega_1/\omega_1$ (thus the symbol $\emptyset$), then only I_{Nb}

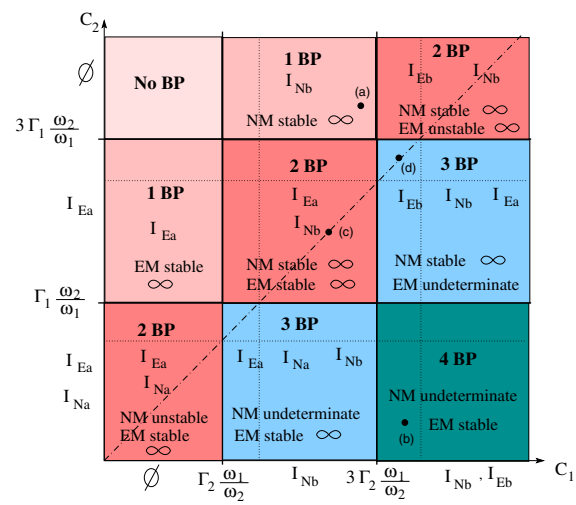

Fig. 5 Type of solutions in the parameter plane (C_1, C_2), for when Γ_1 and Γ_2 are fixed. Specific points labeled **a–d** corresponds to the examples given in Fig. 6a–d. A ∞ sign is represented when the branch of coupled solution is of infinite extent, otherwise the branch is finite

exists for $C_1 > \Gamma_2\omega_1/\omega_1$ and finally both I_{Nb} and I_{Eb} exist for $C_1 > 3\Gamma_2\omega_1/\omega_1$.

The parameter plane exhibits 9 different regions, one with no branch point at all and one with 4 branch points, 2 regions with 1 and 3 branch point, and 3 regions with 2 branch points. In each area, the existing branch point is reported, as well as the stability of the coupled mode, which could be a normal mode (NM) and/or an elliptic mode (EM), following the rule of the value of S_c as compared to either 2 or 2/3. For example, in the two zones where a single branch point exists, there is a region where I_{Nb} exists, thus the coupled solution is a normal mode and it is stable. In the other area, an elliptic mode arises from the branch point and it is also stable. In these two cases, the coupled mode solution branch is infinite and is reported in the chart for each case with the ∞ sign.

In the three regions with two branch points, one can distinguish the upper right region, where both I_{Eb} and I_{Nb} exist. This means that both the NM and EM appear, and are both connected to the B-mode solution. They are also both infinite and the NM is stable while the EM is unstable. Symmetrically, the lower left region shows two coupled modes branching from the A-mode, of infinite size, with NM unstable and EM stable. In the central region, the NM is connected to the B-mode while the EM branches from the A-mode, and both coupled solutions are stable.

In the regions with 3 branch points, the upper right zone is characterized by an EM branch of finite size, since both I_{Ea} and I_{Eb} exist. The stability of the EM is undetermined in this case, since the two cases (stable/unstable) can appear in this area, depending on the parameter values. On the other hand, NM is an infinite branch of stable solution. Symmetrically in the lower left region with 3 branch points, NM is a finite branch of solutions connecting A-mode to B-mode, and its stability cannot be unambiguously determined, whereas EM is stable. Note that the perfect detuned case studied in the previous section falls into this region as illustrated in Fig. 3. Finally when the four branch points exist, the two coupled solutions are of finite extent, EM is stable while the stability of NM cannot be unambiguously determined.

Figure 6 illustrates the preceding analysis by showing various cases. Figure 6a, corresponding to point (a) shown in Fig. 5, is a case where only one branch point exists and give rise to a stable normal mode, emanating from a pitchfork bifurcation on the B-mode. Figure 6b also shows a three-dimensional representation of the solution branches in the space (a, b, ω_{NL}), where 4 branch points are present, giving rise to two stable coupled solutions of finite extent. Note that in this area of the stability chart shown in Fig. 5, the elliptic mode is always stable, however depending on the values one can have either a stable or an unstable normal mode. In Fig. 6b with the selected values of the coefficients, the normal mode is also stable. Figure 6c, d shows the solutions in a Frequency-Energy Plot (FEP), which is possible only when $C_1 = C_2$. Figure 6c shows the shape of the solution branches in a case where two branch points exist, giving rise to two stable coupled solutions of inifinite extent. Finally, in Fig. 6d, three branch points are present, so that the elliptic mode is stable with finite extent, while the solution branch of elliptic mode is stable with infinite extent.

Depending on the cases described above, several geometrical characteristics of the coupled solutions can be drawn out. First, two main topologies can be exhibited. The first possibility for a given coupled solution is to emerge from an uncoupled backbone curve (A-mode or B-mode) through a pitchfork bifurcation and extend to infinity. In Fig. 5, this is shown in all cases having from 1 to 3 branch points and labeled with a ∞ sign. The second possibility for a given coupled solution is to connect the two uncoupled backbones. In this case, two pitchfork bifurcations are necessary. In Fig. 5, they are present only in cases with 3 or 4 branch points. Depending on the stability of the considered coupled solution, the pitchfork bifurcations are either subcritical or supercritical. Secondly, as shown before, the EM branches always emerge from the upper limit, in term of amplitude, of the instability region, *i.e.* the red limit curves of the instability regions obtained with $s = -1$. On the other hand, the NM branches always emerge from its lower limit, the green limit curve of the instability regions obtained with $s = +1$. In a FEP, the obtained topologies are shown in Figs. 6c, d. They are very different from more classical $n : m$ internal resonances that appear as loops in the FEP (see [10, 17]).

2.4 Comparison with a numerical solution

To conclude this section on the theoretical developments, a comparison is drawn out between the analytical solutions derived with the multiple scales

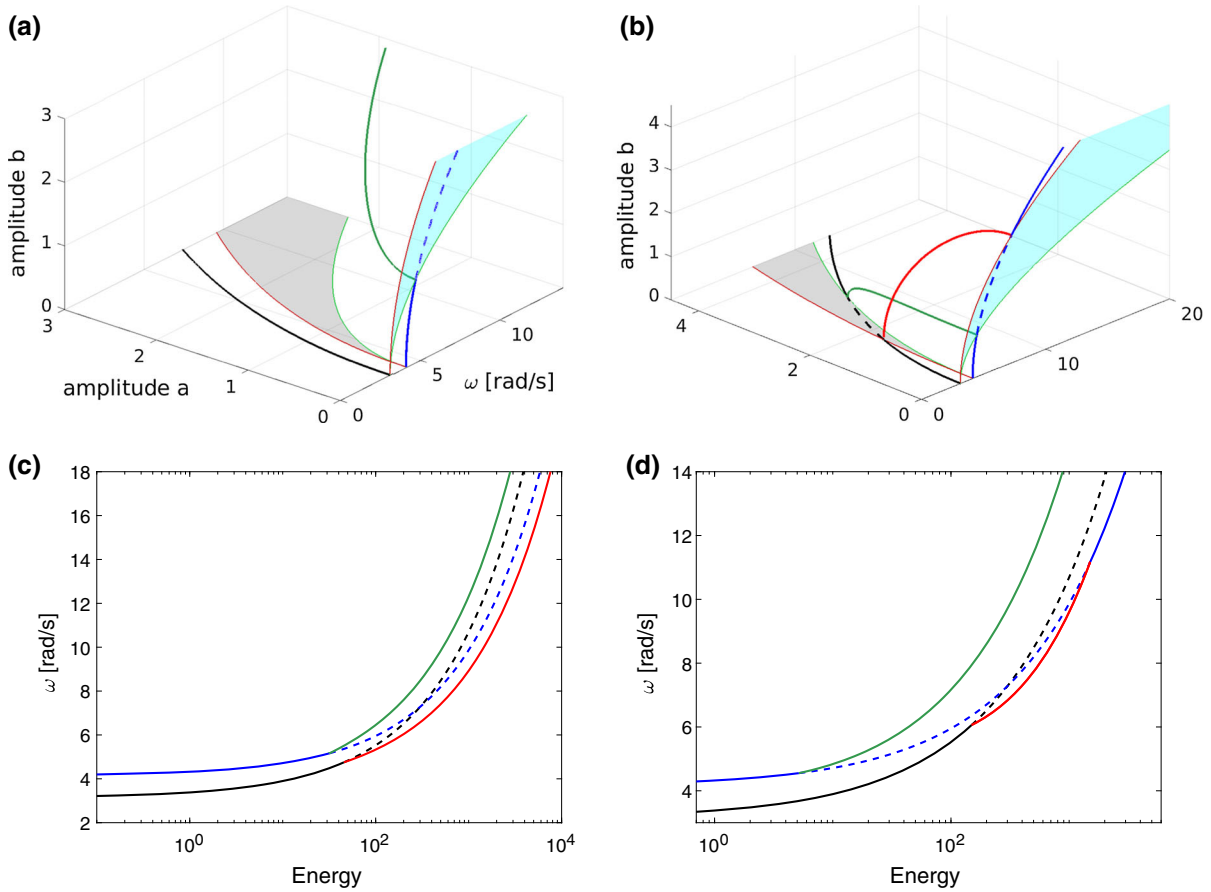

Fig. 6 Miscellaneous solutions for $\Gamma_1 = \Gamma_2 = 1, \omega_1 = \pi$, $\varepsilon = 1$ and $\sigma_1 = 1$. Black line: backbone of the A-mode, blue line: backbone of the B-mode, red line: elliptic mode, green line: normal mode. **a** Case with one branch point for $C_1 = 2, C_2 = 5$, and corresponding to point (**a**) in Fig. 5. **b** Case with four branch points for C_1=3, C_2=1, point (**b**) in Fig. 5. **c** Frequency-Energy plot (FEP) for the case $C_1 = C_2 = 1.5$ with two branch points, point (**c**) in Fig. 5. **d** FEP for the case $C_1 = C_2 = 2.6$ with three branch points, point (**d**) in Fig. 5. (Color figure online)

method and a numerical solution obtained thanks to a continuation method. A pseudo-arc length method, as implemeted in the software AUTO 2000 [8], is used to obtain the numerical reference solution. A key point related to the analytical solution is that the first-order expansion is valid as long as the amplitudes of the responses are smaller than one. For the sake of clarity, all the figures shown in the previous sections have been realised by selecting $\varepsilon = 1$, leading to amplitude values larger than one, preventing direct comparison with the numerical solution. In order to draw out a fair comparison, the coefficients have been reselected as $\varepsilon = 0.1$, $\omega_1 = \pi$ and $\sigma_1 = 1$, so that $\omega_2 = \pi + 0.1$. The nonlinear coefficients have been set to $\Gamma_1 = \Gamma_2 = 10$, $C_1 = 20$ and $C_2 = 5$. For these values, the stability chart given in Fig. 5 predicts a stable elliptic mode of infinite extent and a normal mode of finite extent, which is here found to be unstable.

Figure 7 shows the comparison between analytical and numerical results, where analytical results are reported with a thick line whereas a thin line is used for numerical solutions. As expected, the solutions are almost perfectly identical when the amplitudes are smaller than 1, which is especially true for the solution branch of normal modes, where both solutions are perfectly equal. For all the other branches, one can observe that as soon as the amplitudes are larger than one, a small departure is found between the analytical solution and the numerical solution, as seen on the uncoupled solutions and the branch of coupled elliptic modes. These differences are completely logical and

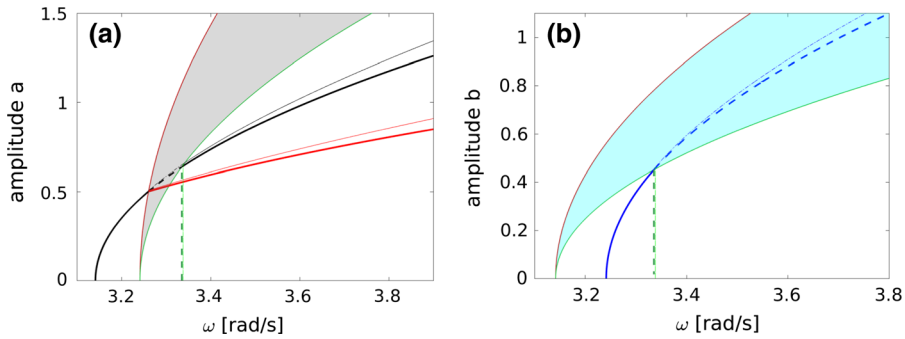

Fig. 7 Comparison between analytical and numerical solution obtained with a pseudo arclength continuation method. Selected parameters are $\Gamma_1 = \Gamma_2 = 10$, $C_1 = 20$, $C_2 = 5$, $\varepsilon = 0.1$, $\omega_1 = 3.14159$, $\omega_2 = 3.24159$. Analytical solutions with thick lines, numerical solutions with thin lines, showing a perfect comparison as long as the amplitudes are smaller than 1. Colour code as in the previous figures: black line: backbone of the A-mode, blue line: backbone of the B-mode, red line: elliptic mode, green line: normal mode. (Color figure online)

in line with the first-order perturbative solution. Note in particular that it could lead to modification of the predictions of bifurcation scenario given by the chart in Fig. 5. Indeed, all the solutions in Fig. 5 are found by comparing the curvature of solution branches at first order defined by parabolas. When amplitudes are larger than one, the curvature is slightly modified by higher-order so that some pitchfork bifurcation points I can move and change the whole picture. Hence the analytical predictions are meant to be very accurate only for small amplitudes, otherwise slight modifications may appear.

3 Experiments

An experimental investigation is also performed in order to illustrate the previous findings, in which the first two companion asymmetric modes of a circular plate are considered. The selected plate is of radius $R = 0.11$m, thickness $h = 1.5$mm, and is made in brass of mass density $\rho = 8486\text{kg m}^{-3}$, Young's modulus $Y = 110$GPa and Poisson ratio $\nu = 0.3$. The responses are measured around the first resonances of the structure, i.e. the two companion asymmetric modes with two nodal diameters. Due to the rotational symmetry of the plate, these modes thus have close eigenfrequencies.

3.1 Experimental setup

The experimental setup is shown in Fig. 8. The plate is hanged horizontally (with respect to gravity) by three

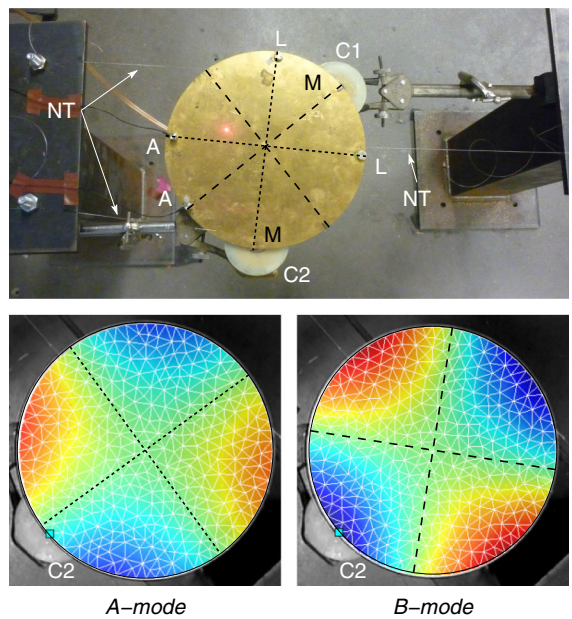

Fig. 8 Investigated structure and operating deflection shapes of the two modes, with detailed positions of the nodal radii (in dashed lines), accelerometers (A), coils (C1, C2), magnets (M), lests (L) and nylon threads (NT). Notice that the orientations of the two bottom figures are different from the upper one, with a rotation of $\simeq 45°$. (Color figure online)

Nylon threads attached in three holes of small radius, equally spaced near its outer edge, to replicate the theoretical free boundary conditions. The excitation system consists of a custom-built non-contact coil/magnet device. The interested reader can refer to [39] for all practical details. It has a very low distorsion rate compared to a traditional shaker excitation, the mechanical forcing considered here is

proportional to the current intensity. A preliminary modal analysis is performed from velocity measurements thanks to a scanning laser vibrometer (Polytec PSV-400). The operating deflection shapes of the two companion modes under interest are shown in Fig. 8 and labeled A-mode and B-mode in accordance with the theoretical part of the article, the A-mode being the one with the lower eigenfrequency. To measure the modal coordinates associated with those two modes, we use two small accelerometers (Brüel & Kjær 4375) glued near the edge of the plate, precisely on a nodal radius of the deformed shapes, to naturally discriminate the effect of the two modes. In this way, each accelerometer measures the oscillation of one mode only. Two neodymium magnets are also glued on the nodal radii of the two modes, so as to allow actuation of each mode separately with the help of a coil.

The plate with no accelerometers and only a single magnet attached (to excite the plate) have eigenfrequencies at 107.3 Hz and 115.8 Hz. To reduce the gap between those two frequencies that arises from the unavoidable imperfections of the system, additional lests (magnets) are placed on the two nodes of A-mode, on both sides of the plate, to reduce the frequency of B-mode. Table 1 shows the effect of all added masses and that the full configuration has closer eigenfrequencies, with a frequency difference of 4.59 Hz instead of 8.5 Hz.

An experimental continuation procedure based on a Phase Locked Loop (PLL) [7] is used to measure the backbone curves as well as the forced responses of the system as shown in Fig. 9. The excitation is an amplified sine signal of frequency Ω sent to the coil, which creates a force proportional to the current intensity denoted as $I(t)$. A real time control system (a dSpace MicroLabBox 1302T), with a control loop mainly based on a proportional/integral controller, adjusts the frequency Ω so that a prescribed phase is obtained between the force excitation signal[1] and the acceleration of one of the modes (called $a_1(t)$ and $a_2(t)$ respectively for the A-mode and B-mode). Due to the nonlinearities, a small harmonic distorsion is often observed in the acceleration signal and the phase estimations are performed on the first harmonic of the signal, as extracted from a homodyne detection. The sampling frequency of the control system is fixed at 50 kHz and for all measurements, the integral and proportional gains of the control loop are respectively fixed at $K_i = 150$ and $K_p = 5$. These values are larger than those used in [7] but avoid the instability regions of the control system in a closed-loop case. It has been shown in [7] that if the system behaves as a single Duffing oscillator, the unstable parts of the forced response are stabilized by the control loop, without changing the systems response in the steady state.

In practice, since only the first harmonics of the signals are measured, we write the current intensity and the two displacement signals at points A and B:

$$\begin{aligned} &I(t) = I_0 \cos \Omega t, \quad w_A(t) = w_1 \cos(\Omega t - \psi_1), \\ &w_B(t) = w_2 \cos(\Omega t - \psi_2). \end{aligned} \tag{24}$$

Then, since the acceleration are measured at points A and B, with amplitudes a_1, a_2 and phases ψ_1, ψ_2 respectively, we obtain the amplitude w_1, w_2 and the phases ϕ_1, ϕ_2 of the displacement signals at points A and B on the plate by:

$$\begin{aligned} &w_1 = \frac{a_1}{\Omega^2}, \quad w_2 = \frac{a_2}{\Omega^2}, \quad \phi_1 \equiv \psi_1 + \pi \ (\mathrm{mod}\ 2\pi), \\ &\phi_2 \equiv \psi_2 + \pi \ (\mathrm{mod}\ 2\pi). \end{aligned} \tag{25}$$

Two distinct measurements can be performed [7]. First, it is possible to measure a given backbone curve by prescribing the phase lag between the displacement and the forcing signals to a fixed value $\phi = -\pi/2$, so as to excite the system in phase resonance. Then, by increasing the forcing amplitude, the control system adjusts the frequency Ω so that ϕ is as close as possible to $-\pi/2$ and Ω is thus theoretically the free oscillation frequency of the associated conservative system. This is because at phase resonance, the forcing exactly cancels the viscous damping forces [30]. The second experiment measures a forced response. In this case, the amplitude of the forcing I_0 to a selected value is prescribed. For a given system, if the phase is a monotonous function of a path parameter on the forced response curve e.g. a Duffing oscillator [7], a phase sweep (between 0 and π for instance) gives the full forced response of the system with the unstable part stabilized (and thus measured) by the control system. These two types of measurements are both applied to the circular plate in the current work.

[1] In practice the current intensity in the coil is measured, and is assumed to be proportional to the actual force with no phase lag.

Table 1 Comparison of the resonance frequencies of the plate, with initial and complete devices

Plate setup	Mode A: f_1 (Hz)	Mode B: f_2 (Hz)	$\Delta f = f_2 - f_1$ (Hz)
Hanged plate + {magnet} ×2	107.3	115.8	8.5
Plate + {magnet + accel.} ×2 + lests	104.66	109.25	4.59

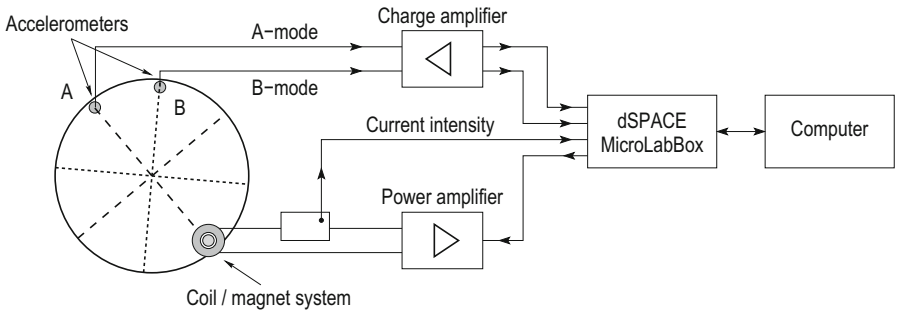

Fig. 9 Scheme of the experimental setup. a_1, a_2 and Q denote the measured accelerometers and the electromechanical excitation, respectively at the inputs and output of the dSpace

3.2 Backbone measurements and identification

The backbone curve of the A-mode is first measured. The plate is excited at a node of B-mode as shown in Fig. 9, so that the modal excitation of the companion B-mode is as small as possible. Then, using the PLL procedure described in the previous section, a phase lag of $\psi_1 = \pi/2$ ($\phi_1 = -\pi/2$) is prescribed and the amplitude of excitation is increased from zero. The black curve in Fig. 10a, b shows the amplitude and phase of the A-mode, w_1 and ψ_1, as a function of the driving frequency Ω, whereas the purple curves shows the amplitude and phase of the B-mode, w_2 and ψ_2. For low amplitudes, a smooth hardening backbone curve is obtained, with the amplitude w_2 of B-mode remaining close to zero (Fig. 10a). This solution branch is thus a part of the (uncoupled) backbone of the A-mode, since no significative response of the B-mode is observed. Then, for $(w_1, \Omega/(2\pi)) \simeq (0.8\text{mm}, 111\text{Hz})$, a change of curvature is observed and w_2 starts to increase from zero. Looking at the phases in Fig. 10b, it is observed that the phase of B-mode locks exactly at $\psi_2 = \psi_1 - \pi/2$. Qualitatively, this part of the response has the features of an elliptic mode, as described theoretically in Sect. 2.2, that emerges from the A-mode after an imperfect pitchfork bifurcation.

In the same manner for the backbones of the A-mode and the EM, the same procedure is applied to obtain the backbone of the B-mode. The plate is excited at an node of the A-mode and the phase of the B-mode is prescribed at $\psi_2 = -\pi/2$ with the driving amplitude increased from zero. A single hardening uncoupled backbone is obtained and shown as a solid blue line in Fig. 11.

With the backbones of the A-mode, B-mode and EM all gathered in Fig. 11, it is possible to estimate the values of the coefficients of the reduced order model of Eq. (1). First, the two eigenfrequencies ω_1 and ω_2 are obtained as the vanishing amplitude limit of the two A-mode and B-mode backbones, at 104.66 Hz and 109.26 Hz. Then, with the curvature of those two uncoupled branches, the coefficients Γ_1 and Γ_2 can be estimated using Eqs. (8) and (9). Finally, the elliptic mode coupled backbone that emerges from the uncoupled A-mode backbone at $\simeq$111 Hz allows the estimation of the two remaining nonlinear coefficients, that are considered equal in this case: $C_1 = C_2$. The fitting of this last coefficient is processed such that:

- From Eq. (22), the intersection between the backbone curve of A-mode and the instability region from which the elliptic mode appears (point I_{Ea}) gives an estimate for coefficient C_2;
- The curvature of the elliptic mode, given by Eq. (17) identifies the coefficient C_1 independently of C_2.

The backbone curves computed with the estimated coefficients are also shown in Fig. 11, as well as the instability regions, computed with Eqs. (8), (9), (17),

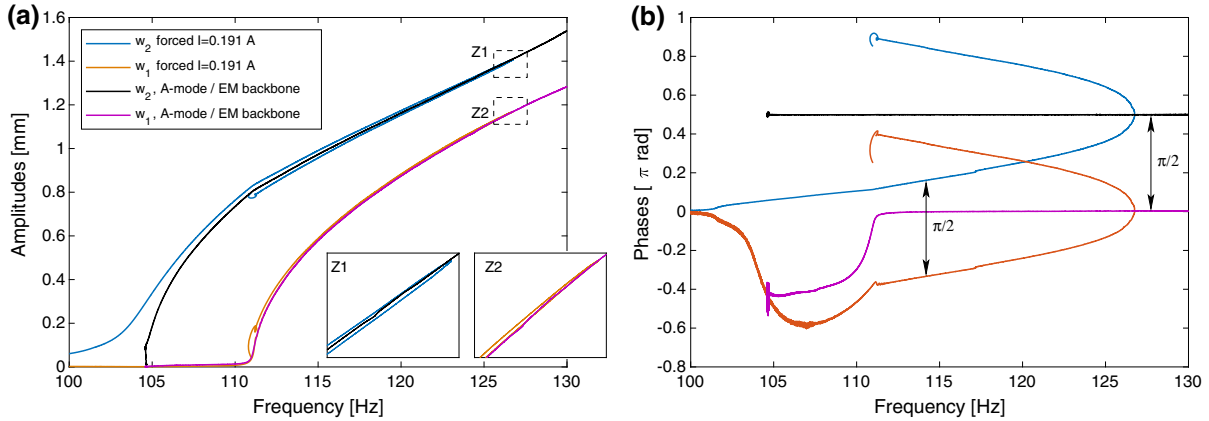

Fig. 10 Amplitudes and phases of the displacement signals of the A and B-mode mode during a phase resonance experiment (black and purple curves, respectively) and during a forced experiment (blue and red curve, respectively; phase sweep at constant driving amplitude of $I_0 = 0.191$A). Some details, around the amplitude resonance of the elliptic mode, are provided (z_1, z_2). (Color figure online)

(36) and (37). An almost perfect agreement is obtained between the experimental measurements and the theoretical results for amplitudes of oscillations up to 1 mm. For higher amplitudes, a slight departure between theoretical predictions and measurements is observed, which is probably due to the first-order solution used in the calculations, valid only for small amplitudes of motion.

It must also be noted that the model identification proposed here can be viewed as an extension to the case of a 1:1 internal resonance of the general procedure proposed in [7]. The model is obtained by a normal form reduction (restricted to a 4 nonlinear terms perfect case) and identified via backbone curves obtained from experimental continuation. It is, to the knowledge of the author, a first (but modest) attempt of identification of a nonlinear model with modes in internal resonance, whereas other contributions use the forced responses [23, 39, 41]. It will be seen in the next section that this parameter identification is also robust in the sense that the results can be easily extended to forced vibrations.

The identified coefficients are now compared to analytical values computed from a nonlinear plate

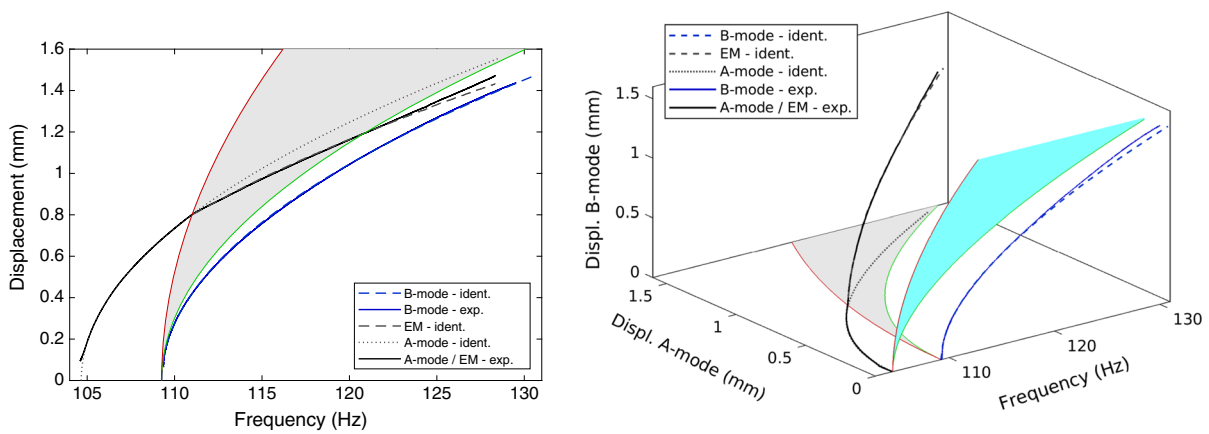

Fig. 11 Experimentally identified backbones and stability curves: amplitudes w_1 and w_2 of A and B-mode as a function of frequency Ω. Black solid line: measured backbone curve of A-mode (A-mode exp., before the stability limit, in red) and elliptical mode (EM—exp., after the stability limit). Blue solid line: experimental backbone curve of B-mode (B-mode exp.). Black dotted and blue dashed lines: identified backbones of respectively A and B-modes in uncoupled regime (A-mode ident., B-mode ident.). Black dashed line: identified backbone of the coupled elliptic mode (EM—ident.). (Color figure online)

model, founded on the Kirchhoff-Love kinematics and the von Kármán strain—displacement law. A complete derivation and numerical results can be found in [10, 45], where a dimensionless form of the nonlinear plate equations is used to obtain the general system of Eq. (1). Due to the choosen locations of the accelerometers, the physical parameters are considered proportional to the modal coordinates. Consequently, the following relationships between physical and dimensionless values are used to perform the adjustment of the model parameters:

$$f = \frac{h}{2\pi R^2}\sqrt{\frac{E}{12\rho(1-\nu^2)}}\bar{\omega}, \quad w_1 = \Phi(r_{\text{meas}})\frac{h^2}{R}2a,$$
$$w_2 = \Phi(r_{\text{meas}})\frac{h^2}{R}2b, \quad \varepsilon = \frac{12(1-\nu^2)h^2}{R^2}, \tag{26}$$

where f refers to a frequency in Hz related to a dimensionless angular frequency $\bar{\omega}$, $\Phi(r_{\text{meas}})$ is the theoretical amplitude of the mode shape of the considered mode, defined with Bessel functions (see [45]) at the radius r_{meas} of location of the accelerometers. One has to notice the factor 2 comes from the definition of w_1 and a (resp. w_2 and b) in Eqs. (7) and (24).

According to this scaling, the dimensionless values of coefficients Γ_1, Γ_2, $C_1 = C_2$ are gathered in Table 2, from both the theory [45] and the present estimated values. The estimated nonlinear coefficients are a little smaller than the theoretical values, with an error of the order of 5%, 10% and 20% for the coefficient Γ_1, coefficient Γ_2 and the 2 coefficients C_1 and C_2 respectively. These differences with the numerical values can be explained by the imperfections, inherent to the plate but also the added masses (accelerometers, magnets). The nonlinear coefficients are sensitive to the mode shapes, in particular to the differences between the nodal and anti-nodal diameters compared to those of a perfect plate. Similar results have been found in [39].

Due to the imperfections, the pitchfork bifurcation at 110 Hz leading to the coupled elliptic mode is also imperfect; thus a single continuous stable branch is found and naturally followed by the PLL. The second stable coupled branch (with almost the same amplitude and a phase $\psi_2 = \psi_1 + \pi/2$), should be isolated from the main branch and connected to the uncoupled unstable A-mode backbone by a saddle-node bifurcation. It has not been possible to initialize the PLL procedure on one of the isolated branch to measure them, as it has been done in [39]. Moreover, preliminary numerical investigations on the model of Sect. 2, shows that whatever the value of the coefficients, only perfect pitchfork bifurcations are found. This suggests that the imperfections of the plate should be taken into account by small nonzero added nonlinear cubic terms in the model (e.g. the X_2^3 and $X_1^2X_2$ terms in Eq. (1a) and the X_1^3 and $X_2^2X_1$ terms in Eq. (1b), thus extending the analysis to eight parameters for the nonlinear coefficients. This is logical as adding those new terms in the equations prevent the uncoupled solutions from existing, since invariant-breaking terms, in the sense given in [43], are now present. Consequently, perfect bifurcation cases exist with those new terms, which has been clearly observed with numerical investigations using continuation methods. The detailed analysis of this transition to imperfect bifurcations is however left for further studies.

3.3 Forced response around A-mode and PLL behavior

In parallel to the backbone curve measurements of the previous section, forced responses have also been measured by the PLL control system, by keeping the amplitude of forcing constant and sweeping the phase of the directly excited mode from 0 to π. These supplementary measurements demonstrate that the PLL control system is also able to observe the 1:1 internal resonance in the case of the forced responses. In particular, the entire response curve could be measured only if the controlled phase is monotonous. Figure 10 shows a typical forced response when the driving point is chosen on a node of the B-mode to mainly drive the A-mode. Similar responses than those predicted and measured in [39, 45] are obtained, with a phase difference of $\psi_2 - \psi_1 = \pi/2$ between A and B-mode in the coupled part, a characteristic of a forced elliptic mode giving rise to a rotating travelling wave. Two features are noteworthy. First, the forced response lies in the vicinity of the backbones, with a crossing at the phase resonance of the coupled branch ($\psi_1 = \pi/2$), which stands close to the amplitude resonance. Second, the unstable part is stabilized by

Table 2 Identified values of frequencies, modal dampings and nonlinear coefficients by adjusting theory with experiments. The theoretical value of those coefficients, from [45], are also given

	Identified								Theory
	f_1 (Hz)	f_2 (Hz)	$\xi_1(\%)$	$\xi_2(\%)$	Γ_1	Γ_2	C_1	C_2	$\Gamma_1 = \Gamma_2 = C_1 = C_2$
Free	104.66	109.26	–	–	1.80	1.68	1.55	1.55	1.89
Forced	104.90	109.01	0.13	0.06	1.80	1.58	1.85	1.58	1.89

the PLL control loop on a large part of the coupled response, as discussed in the following.

Figure 12 displays the backbone of the A-mode and several forced responses, for three excitations levels. First, the same qualitative behaviour is obtained, with the nonlinear forced responses, shown as green and yellow curves, distributed around the backbone curve both for the uncoupled solution and after the emergence of the 1:1 internal resonance. Secondly, for the same response curves, the PLL control loop is not able to stabilize the whole forced response in a single phase sweep, as it would be the case for a Duffing oscillator [7]. Indeed, a first branch is obtained by an increasing phase sweep from $\psi_1 = 0$ corresponding to point C in Fig. 12. Then, point D is reached, with the emergence of the 1:1 interaction, which is theoretically stable until the saddle-node bifurcation at point E on the green curve. Then, further increasing the phase leads to the measurement of a theoretical unstable coupled branch, which is stabilized by the PLL until point F in which the control loop loses its stability. It is possible to measure another branch starting from point G with a phase close to π and doing a decreasing phase sweep, to first reach point H with a saddle-node bifurcation and then point F where the control loop loses its stability.

To discuss this instability of the control system in forced regime, the experimental results are compared to the numerical simulations obtained using the continuation software Manlab [2, 11], that enables the simulation of periodic responses of system like Eq. (27) using the harmonic balance method and an asymptotic numerical method. The stability of the branches is obtained by the Hill method [18]. The values of the parameters used for the simulation are gathered in the last row of Table 2. The values common with the free response case have been slightly changed for a better fit on the experiments. Then, modal damping factors (dimensionless), defined as $\xi_1 = \varepsilon\mu_1/\omega_1$ and $\xi_2 = \varepsilon\mu_2/\omega_2$, have been estimated by a half power bandwidth method on linear (small amplitude) frequency response functions. Finally, the forcing amplitudes have been chosen such that $F_1 \gg F_2$, with $F_1 = 5.97$ and $F_2 = F_1/35.0$, with a slight non zero forcing of B-mode due to experimental imperfections.

The computed forced responses are presented in Fig. 13. A remarkable comparison is obtained between theory and experiments. However, the simulations show precisely the topology of all the unstable branches, especially the uncoupled resonance of the A-mode. Its unstable part is connected to the rest of the diagram through two pitchfork bifurcations, at points D and F in Fig. 13. Because of the nonzero value of F_2, these pitchfork bifurcations are imperfect. The main result is that the PLL control loop loses its stability precisely at the pitchfork of point F, where the unstable uncoupled A-mode branch is connected to the rest of the diagram. For a reason out of the scope of this paper, the PLL control system is not able to branch into the coupled regime from the uncoupled one and inversely at point F. It must be noticed that the stability of the PLL control loop has been theoretically proved only with a single Duffing oscillator in [7]. This study remains to be extended to the present case of a 1:1 internal resonance. A particular focus on the phase paths of the two oscillators needs to be performed. Indeed, the particular behaviour of the PLL control loop observed in this section could be explained by a complex topology of the phases, not compatible with the monotonous path prescribed in these experiments.

4 Conclusion

This paper adresses the theoretical analysis and the experimental investigations on a system with two coupled oscillators of cubic nonlinearities featuring

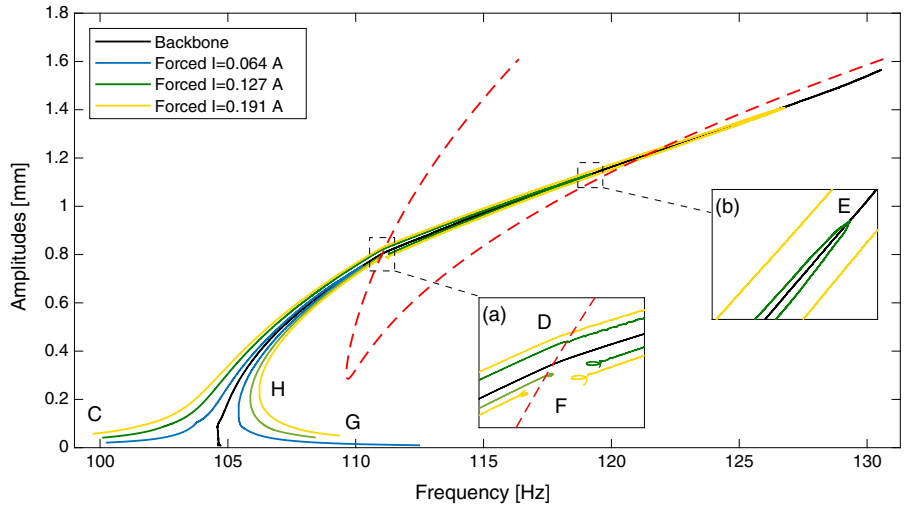

Fig. 12 Experimental forced responses around the backbone of the A-mode. Dashed red line: limits of the instability regions, computed with the identified parameters of Table 2. (Color figure online)

1:1 internal resonance. The coupled and uncoupled solutions of the nonlinear system are derived by using a multiple-scale analysis. The main outcomes of the analytical results offer a complete view of the bifurcation scenario thanks to the derivation of the analytical expressions of the instability regions, that has never been written out in the previous investigations on the 1:1 resonance in free vibrations. An extension to the results by Manevitch and Manevitch [21] is also provided by taking into account 4 nonlinear coupling coefficients as parameters. Depending on the parameter values, nine possible bifurcation scenarios have been established, with different topological configurations including

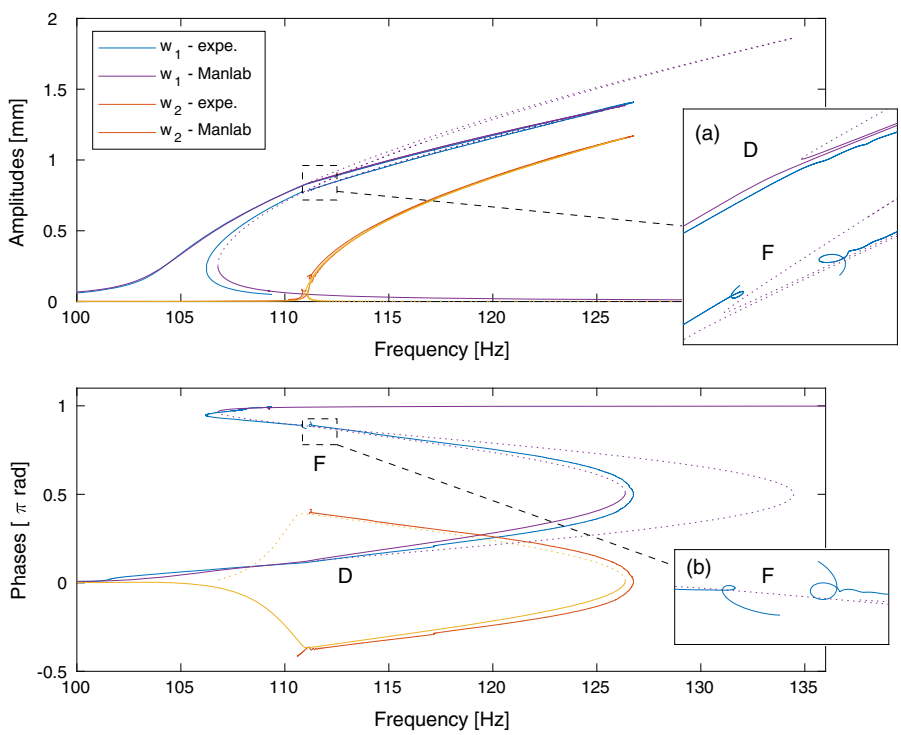

Fig. 13 Experimental (expe.) amplitudes and phases of the displacements around A-mode response in forced regime under current $I_0 = 0.191$ A. Numerical corresponding response, computed with Manlab, with the estimated parameters. The theoretical unstable branches are plot in dashed line. (Color figure online)

supercritical or subcritical pitchfork, two kinds of coupled solutions (elliptic and normal modes), with solution branches either of finite or infinite extent. The measurements on two companion configurations of a circular plate exhibit one bifurcation point, from which a coupled elliptic mode emerges. The estimation of the nonlinear coefficients leads to identification of the corresponding scenario, showing that the experimental setup does not allow measurement of all the existing solutions. The behaviour of the PLL system in the forced regime has also been commented showing its difficulty in following a single run of a complete bifurcation diagram when a 1:1 resonance is activated. This behaviour is found to be different from the one observed when following a simple Duffing equation, necessitating further research in order to give a better control on the system to measure all solutions smoothly. Imperfect bifurcations has been also discussed as a key point to explain the slight differences between the theory and the experiments, and it has been underlined that in free vibrations, imperfect pitchfork bifurcations are observed only when taking into account the other nonlinear coupling coefficients than the four retained in this study. This particular point may call for further dedicated research to shed light on this specific behaviour.

Acknowledgements A part of this study was funded by the French Ministry of Research and Arts et Métiers through the PhD grant of the first author. Another part of the research work presented in this paper has been realized during the doctoral thesis of Jin-Jack Tan in IMSIA, ENSTA Paris, and was funded by the european commission within the Initial Training Network (ITN) Marie Curie action project BATWOMAN, under the seventh framework program (EC grant Agreement No. 605867).

Compliance with ethical standards

Conflict of interest The authors declare that they have no conflict of interest.

Appendix 1: derivation of first-order equations

This appendix gives the full detail of the derivation of the first-order slow-scale equations for the system of cubic oscillators featuring 1:1 internal resonance using the multiple scales method. The derivation is written for the forced and damped problem and is then finally reduced to free vibration by cancelling the forcing and damping terms. This allows us to give a unified presentation for the two cases, following closely the derivation shown in [45]. It is also mandatory for our presentation since the derivation of the instability region for the free vibration is derived from the forced and damped case, as explained below.

The starting point is thus the following equations of motion:

$$\ddot{X}_1 + \omega_1^2 X_1 + \varepsilon\left[2\mu_1\dot{X}_1 + \Gamma_1 X_1^3 + C_1 X_1 X_2^2\right] = \varepsilon F_1 \cos\Omega t, \tag{27a}$$

$$\ddot{X}_2 + \omega_2^2 X_2 + \varepsilon\left[2\mu_2\dot{X}_2 + \Gamma_2 X_2^3 + C_2 X_2 X_1^2\right] = \varepsilon F_2 \cos\Omega t. \tag{27b}$$

These two equations generalizes the case of free vibration considered in (1), by adding two different damping factors for each oscillator, μ_1 and μ_2, and two forcing terms with amplitudes F_1 and F_2, scaled at order ε since the primary resonance is investigated. These equations are close to those used in [45], except that two distinct damping terms are considered instead of a single one $\mu = \mu_1 = \mu_2$ selected in [45]. Note also that in [45], the nonlinear stiffness terms were at the right-hand side of the equations of motions, so that the comparison can be drawn by simply changing the signs of Γ_1, Γ_2, C_1 and C_2.

The two detunings are introduced as

$$\omega_2 = \omega_1 + \varepsilon\sigma_1, \tag{28a}$$

$$\Omega = \omega_1 + \varepsilon\sigma_2. \tag{28b}$$

The first detuning σ_1 quantifies the 1:1 internal resonance, while σ_2 expresses the fact that a primary resonance is investigated so that $\Omega \simeq \omega_1$. The multiple scales method is introduced, with $T_0 = t$ a fast time scale and $T_1 = \varepsilon t$ a slow time scale. The unknown are expanded as $X_i = X_{i1}(T_0, T_1) + \varepsilon X_{i2}(T_0, T_1)$. The first-order solution is easy to find and reads:

$$X_{11} = A(T_1)\exp(i\omega_1 T_0) + c.c., \tag{29a}$$

$$X_{21} = B(T_1)\exp(i\omega_2 T_0) + c.c., \tag{29b}$$

where $c.c.$ stands for complex conjugate. The solvability conditions write, for the two unknown complex amplitudes $A(T_1)$ and $B(T_1)$:

$$-2i\omega_1(A' + \mu_1 A) - 3\Gamma_1 A^2 \bar{A} - C_1(\bar{A}B^2\,\mathrm{e}^{2i\sigma_1 T_1} + 2AB\bar{B}) + \frac{F_1}{2}\,\mathrm{e}^{i\sigma_2 T_1} = 0, \tag{30a}$$

$$-2i\omega_2(B' + \mu_2 B) - 3\Gamma_2 B^2 \bar{B} - C_2(\bar{B}A^2\,\mathrm{e}^{-2i\sigma_1 T_1} + 2BA\bar{A}) + \frac{F_2}{2}\,\mathrm{e}^{i(\sigma_2-\sigma_1)T_1} = 0, \tag{30b}$$

where $(\,)'$ denotes the derivative with respect to the slow time scale T_1. These two equations can be rewritten by considering the polar form for the two unknowns, such that $A = a(T_1)\exp(i\alpha(T_1))$ and $B = b(T_1)\exp(i\beta(T_1))$. The non-autonomous system for the amplitude and phases finally writes:

$$a' = -\mu_1 a - \frac{C_1}{2\omega_1} ab^2 \sin(2\beta - 2\alpha + 2\sigma_1 T_1) + \frac{F_1}{4\omega_1}\sin(\sigma_2 T_1 - \alpha), \tag{31a}$$

$$\alpha' = \frac{3\Gamma_1}{2\omega_1}a^2 + \frac{C_1}{2\omega_1}b^2(2 + \cos(2\beta - 2\alpha + 2\sigma_1 T_1)) - \frac{F_1}{4\omega_1 a}\cos(\sigma_2 T_1 - \alpha), \tag{31b}$$

$$b' = -\mu_2 b - \frac{C_2}{2\omega_2} ba^2 \sin(-2\beta + 2\alpha - 2\sigma_1 T_1) + \frac{F_2}{4\omega_2}\sin((\sigma_2 - \sigma_1)T_1 - \beta), \tag{31c}$$

$$\beta' = \frac{3\Gamma_2}{2\omega_2}b^2 + \frac{C_2}{2\omega_2}a^2(2 + \cos(-2\beta + 2\alpha - 2\sigma_1 T_1)) - \frac{F_2}{4\omega_2 b}\cos((\sigma_2 - \sigma_1)T_1 - \beta). \tag{31d}$$

Note that in order to make the system (31) autonomous, one needs to introduce the following two additional variables

$$\gamma_1 = \sigma_2 T_1 - \alpha, \tag{32a}$$

$$\gamma_2 = (\sigma_2 - \sigma_1)T_1 - \beta. \tag{32b}$$

When forcing and damping terms are removed, Eq. (31) depends on only one angular variable, so that numerous different choices can be selected in order to make the system autonomous. In order to stay close to the notations used for the forced and damped system, the following change of coordinate is selected as:

$$\gamma_1 = -\alpha, \tag{33a}$$

$$\gamma_2 = -\sigma_1 T_1 - \beta. \tag{33b}$$

This choice leads to the autonomous system given in Sect. 2, Eq. (6).

Appendix 2: instability region for the uncoupled solutions

In this section we derive the instability region of the uncoupled solutions for the free vibration case, from the analysis of the damped/forced system. The starting point is the instability regions derived in [39] for the forced/damped case, *i.e.* for the system (31), made autonomous using change of variable from Eq. (32). The analysis led in [45] shows that uncoupled solution where only the first mode is excited is unstable when this relationship is fulfilled :

$$\sigma_2 = \sigma_1 + \frac{C_2 a^2}{\omega_2}\sqrt{\frac{C_2^2 a^4}{3\omega_2^2} - \mu^2} \tag{34}$$

Cancelling the damping by letting $\mu = 0$ in this equation leads to

$$\sigma_2 = \sigma_1 + (2 + s)\frac{C_2 a^2}{\omega_2} \quad \text{with } s = \pm 1. \tag{35}$$

The last step is to replace σ_2, which is defined by (28b). However cancelling the forcing would result in Ω being undefined. Instead, one needs to map Ω to the nonlinear oscillation frequency in the free regime. σ_2 is then the detuning allowing one to express this nonlinear frequency as a function of the linear eigenfrequency with $\omega_{NL} = \omega_1 + \varepsilon\sigma_2$. Replacing σ_2 with its expression as given by Eq. (35), one can finally obtain:

$$\omega_{NL} = \omega_2 + \varepsilon(2 + s)\frac{C_2 a^2}{\omega_2} \quad \text{with } s = \pm 1. \tag{36}$$

This equation shows that as soon as the nonlinear frequency of A-mode enters the region delimited by the two curves obtained with $s = \pm 1$, then the

uncoupled solution becomes unstable. In order to derive the instability region for the B-mode, the same reasoning is applied using symmetric relationships, leading to:

$$\omega_{NL} = \omega_1 + \varepsilon(2+s)\frac{C_1 b^2}{\omega_1} \quad \text{with } s = \pm 1. \tag{37}$$

Appendix 3: stability of the coupled solutions

The stability of the coupled solution is derived classically from the jacobian matric of (6). The general jacobian $\mathcal{J}$ reads, with $S_\gamma = \sin 2(\gamma_1 - \gamma_2)$ and $C_\gamma = \cos 2(\gamma_1 - \gamma_2)$ in order to ease notations:

$$\mathcal{J} = \begin{pmatrix} -\frac{C_1}{2\omega_1} b^2 S_\gamma & -\frac{C_1}{\omega_1} ab^2 C_\gamma & -\frac{C_1}{\omega_1} abS_\gamma & \frac{C_1}{\omega_1} ab^2 C_\gamma \\ -\frac{3\Gamma_1}{\omega_1} a & \frac{C_1}{\omega_1} b^2 S_\gamma & -\frac{C_1}{\omega_1} b(2+C_\gamma) & -\frac{C_1}{\omega_1} b^2 S_\gamma \\ \frac{C_2}{\omega_2} abS_\gamma & \frac{C_2}{\omega_2} ba^2 C_\gamma & \frac{C_2}{2\omega_2} a^2 S_\gamma & -\frac{C_2}{\omega_2} ba^2 C_\gamma \\ -\frac{C_2}{\omega_2} a(2+C_\gamma) & \frac{C_2}{\omega_2} a^2 S_\gamma & -\frac{3\Gamma_2}{\omega_2} b & -\frac{C_2}{\omega_2} a^2 S_\gamma \end{pmatrix}. \tag{38}$$

The coupled solutions are characterized by specific relationships on the angles leading to simplification of $\mathcal{J}$. Indeed one has $\sin 2(\gamma_1 - \gamma_2) = 0$ and $\cos 2(\gamma_1 - \gamma_2) = s = \pm 1$. With these simplifications the 4×4 determinant of the jacobian matrix $\mathcal{D} = \det(\mathcal{J} - \lambda \mathcal{I})$ with $\mathcal{I}$ the identity matrix can be analytically derived as:

$$\mathcal{D} = \lambda^2 \left[\lambda^2 - 3a^2 b^2 s \left(\frac{\Gamma_2 C_2}{\omega_2^2} + \frac{\Gamma_1 C_1}{\omega_1^2} \right) + 2\frac{C_1 C_2}{\omega_1 \omega_2} b^2 a^2 s(2+s) \right]. \tag{39}$$

Two eigenvalues are found to be zero which is logical for coupled solutions in four-dimensional phase space. The two other eigenvalues are solutions of

$$\lambda^2 = 3a^2 b^2 s \left[\frac{\Gamma_2 C_2}{\omega_2^2} + \frac{\Gamma_1 C_1}{\omega_1^2} - \frac{2}{3}\frac{C_1 C_2}{\omega_1 \omega_2}(2+s) \right], \tag{40}$$

with $s = +1$ for normal mode and $s = -1$ for elliptic mode. Each mode (normal or alliptic) is stable as long as $\lambda^2 < 0$, which leads to the conclusion that stablity is governed only by the value of the scalar $S_c = \frac{\Gamma_1 \omega_2}{C_2 \omega_1} + \frac{\Gamma_2 \omega_1}{C_1 \omega_2}$, the normal mode being stable as long as $S_c < 2$, and the elliptic mode as long as $S_c > 2/3$.

Appendix 4: parametric study: bifurcation scenario in the particular case without detuning

In this appendix, the particular case of perfectly equal eigenfrequencies $\omega_1 = \omega_2$ with a vanishing detuning $\sigma_1 = 0$, is considered. In this case, the amplitude values for which the branch points I_{Ea}, I_{Na}, I_{Eb} and I_{Nb} (as defined in Eqs. (22) and (23)) are equal to zero: this means that the coupled solutions could exist from a vanishing amplitude. This is the direct consequence of the fact that, as $\sigma_1 = 0$, the gaps between the starting point of the A-mode and the B-mode backbone curves and their instability regions, does not exist anymore. The second consequence is also that uncoupled solutions are either always stable or always unstable, whatever the amplitude. Considering the coupled solutions, cancelling the values of all branch points does not mean that NM and EM always exist. Indeed, Eq (14), which defines the amplitude relationships for coupled solutions, rewrites with $\sigma_1 = 0$

$$(3\Gamma_1 - (2+s)C_2)a^2 = (3\Gamma_2 - (2+s)C_1)b^2, \tag{41}$$

with $s = \pm 1$ for NM and EM. Consequently coupled solutions can exist if and only if the respective coefficients in front of the square amplitude have the same sign.

The stability chart that gives all possible solutions as function of the nonlinear coefficients is thus modified and shown in Fig. 14a. The main difference with the detuned case where $\sigma_1 > 0$ is that the coupled solutions of finite extent can not exist anymore since all branch points have the same vanishing amplitude. This leads to modification of the lower right part of the stability chart to make it symmetric. The possible cases are discussed as function of the stability of the uncoupled mode, reported in Fig. 14a on the vertical and horizontal axes. Four cases exist:

- **Case 1** *A-mode and B-mode are stable*. This means that the backbone curve of each uncoupled solution is outside its instability region. It corresponds to the four edges of the stablity chart, in upper left, upper right, lower left and lower right regions. Two cases are then possible:
  - Case 1.1: if $3\Gamma_1 < C_2$ and $\Gamma_2 > C_1$, or if $3\Gamma_2 < C_1$ and $\Gamma_1 > C_2$. This case means that the backbone curve of the A-mode stays on the left of the instablity region while backbone

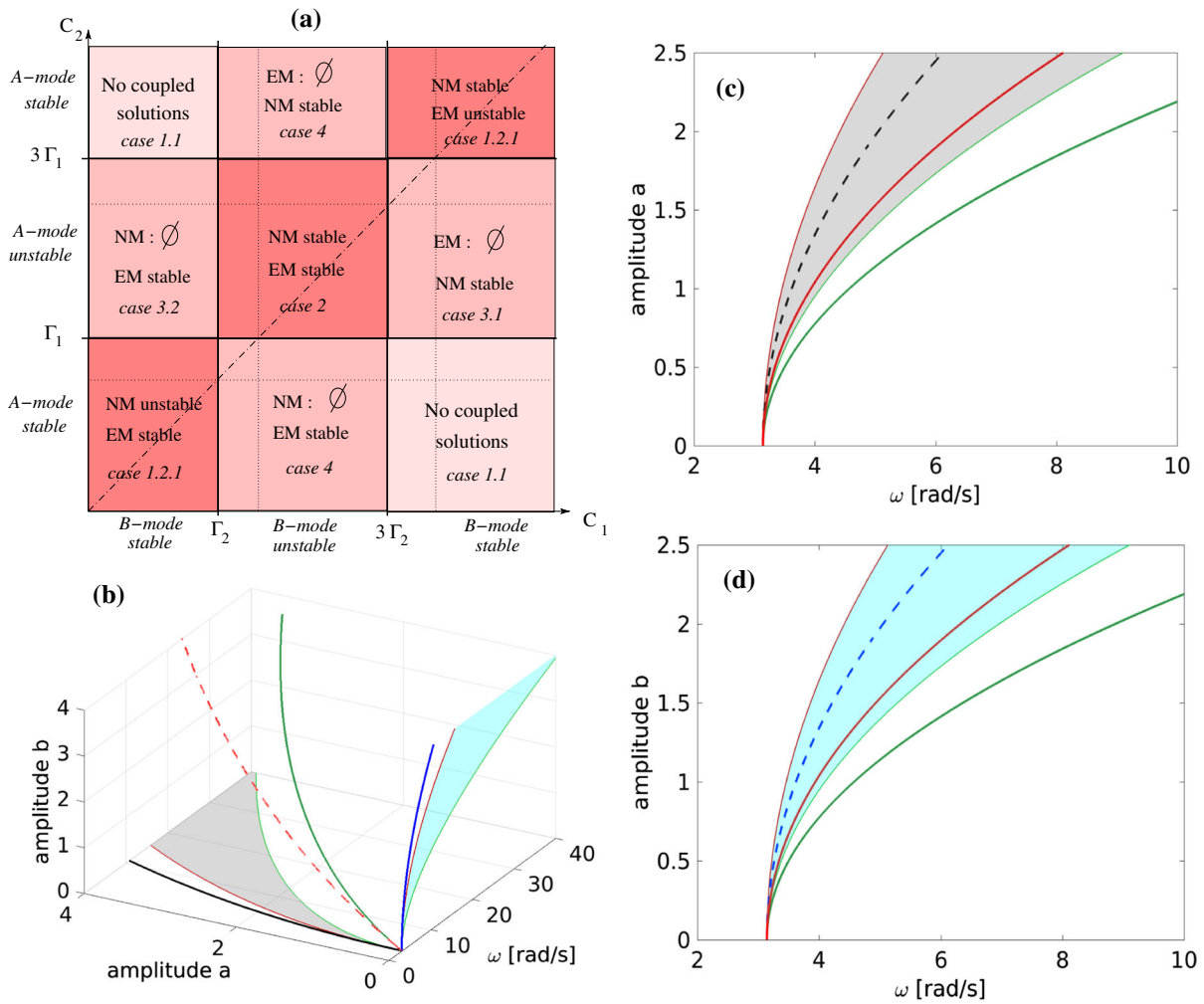

Fig. 14 Stability analysis and bifurcation scenario in the case $\sigma_1 = 0$, with fixed parameters as $\omega_1 = \omega_2 = \pi$, $\Gamma_1 = \Gamma_2 = 1$. **a** stability chart showing the possible solutions when varying the values of the coupling coefficients C_1 and C_2. **b** Three-dimensional representation of the solution branches in space (ω, a, b), for $C_1 = C_2 = 5$. **c–d** Two-dimensional projections in the planes (ω, a) and (ω, b) for the case $C_1 = C_2 = 25$. (Color figure online)

curve of the B-mode is on the right (or vice-versa). Then in this case the coefficients of Eq.(41) have opposite signs, thus no coupled solutions exist.

– Case 1.2: if $3\Gamma_1 < C_2$ and $3\Gamma_2 < C_1$ (case 1.2.1), or if $\Gamma_1 > C_2$ and $\Gamma_2 > C_1$ (case 1.2.2), the backbone curves of the A-mode and the B-mode are respectively on the same side of their instability regions. Then in this case both coupled solutions exist, and inspection of the values of S_c indicates that in case 1.2.1 NM is stable while EM is unstable, and case 1.2.2 leads to the contrary with NM unstable and EM stable.

– **Case 2** *The A-mode and the B-mode are unstable*. This means that each backbone curve is totally inside the instability region, so that $C_2/3 < \Gamma_1 < C_2$ and $C_1/3 < \Gamma_2 < C_1$. Then in this case both coupled solutions exist and are stable.

– **Case 3** *The A-mode is unstable and the B-mode is stable*. The instability of the A-mode is obtained thanks to the condition $C_2/3 < \Gamma_1 < C_2$. Two subcases are then possible:

  - If $3\Gamma_2 < C1$, then EM does not exist, only NM is possible and is stable (case 3.1).
  - If $\Gamma_2 > C_1$, then NM does not exist, only EM is possible and is stable (case 3.2).
- **Case 4** *The B-mode is stable and the A-mode is unstable*. This case can be simply deduced from the previous one by symmetry (changing the indices $1 \rightleftarrows 2$).

Figure 14b illustrates a case in the upper right region of the stability chart, in which both the A-mode and the B-mode are stable and the two coupled solutions exist: the NM is stable while the EM is unstable. Finally Fig. 14c, d shows the projection on the (ω, a) and (ω, b) for the case in the central region where both uncoupled solutions are unstable. In this case, the only stable solutions are the coupled branches, and both EM and NM are stable.

References

1. Afaneh AA, Ibrahim RA (1993) Nonlinear response of an initially buckled beam with 1:1 internal resonance to sinusoidal excitation. Nonlinear Dyn 4(6):547–571
2. Arquier R, Karkar S, Lazarus A, Thomas O, Vergez C, Cochelin B (2005–2011) Manlab 2.0: an interactive path-following and bifurcation analysis software. Technical report, Laboratoire de Mécanique et d'Acoustique, CNRS. http://manlab.lma.cnrs-mrs.fr. Accessed 3 Sep 2019
3. Barton DAW (2017) Control-based continuation: bifurcation and stability analysis for physical experiments. Mech Syst Signal Process 84:54–64
4. Benedettini F, Rega G, Alaggio R (1995) Non-linear oscillations of a four-degree-of-freedom model of a suspended cable under multiple internal resonance conditions. J Sound Vib 182(5):775–798
5. Cammarano A, Hill TL, Neild SA, Wagg DJ (2014) Bifurcations of backbone curves for systems of coupled nonlinear two mass oscillator. Nonlinear Dyn 77(1):311–320
6. Chang SI, Bajaj AK, Krousgrill CM (1993) Non-linear vibrations and chaos in harmonically excited rectangular plates with one-to-one internal resonance. Non-linear Dyn 4:433–460
7. Denis V, Jossic M, Giraud-Audine C, Chomette B, Renault A, Thomas O (2018) Identication of nonlinear modes using phase-locked-loop experimental continuation and normal form. Mech Syst Signal Process 106:430–452
8. Doedel E, Paffenroth R, Champneys A, Fairgrieve T, Kuznetsov Y, Oldeman B, Sandstede B, Wang X (2002) Auto 2000: continuation and bifurcation software for ordinary differential equations. Technical report, Concordia University
9. Evensen DA (1968) Influence of nonlinearities on the degenerate vibration modes of a square plate. J Acoust Soc Am 44(1):84–89
10. Givois A, Grolet A, Thomas O, Deü JF (2019) On the frequency response computation of geometrically nonlinear flat structures using reduced-order finite element models. Nonlinear Dyn 97(2):1747–1781
11. Guillot L, Cochelin B, Vergez C (2018) A generic and efficient Taylor series based continuation method using aquadratic recast of smooth nonlinear systems. Int J Numer Methods Eng 9(4):261–280
12. Haddow AG, Barr ADS, Mook D (1984) Theoretical and experimental study of modal interaction in a two-degree-of-freedom structure. J Sound Vib 97:451–473
13. Hanson RJ, Anderson JM, Macomber HK (1994) Measurements of nonlinear effects in a driven vibrating wire. J Acoust Soc Am 96(3):1549–1556
14. Harrison H (1948) Plane and circular motion of a string. J Acoust Soc Am 20(6):874–875
15. Iooss G, Adelmeyer M (1998) Topics in bifurcation theory, 2nd edn. World scientific, New-York
16. Jossic M, Thomas O, Denis V, Chomette B, Mamou-Mani A, Roze D (2018) Effects of internal resonances in the pitch glide of chinese gongs. J Acoust Soc Am 144(1):431–442
17. Kerschen G, Peeters M, Golinval JC, Vakakis AF (2009) Nonlinear normal modes, part I: a useful framework for the structural dynamicist. Mech Syst Signal Process 23(1):170–194
18. Lazarus A, Thomas O (2010) A harmonic-based method for computing the stability of periodic solutions of dynamical systems. Comptes Rendus Mécanique 338(9):510–517
19. Lewandowski R (1994) Solutions with bifurcation points for free vibration of beams: an analytical approach. J Sound Vib 177(2):239–249
20. Lewandowski R (1996) On beams membranes and plates vibration backbone curves in cases of internal resonance. Meccanica 31(3):323–346
21. Manevitch AI, Manevitch LI (2003) Free oscillations in conservative and dissipative symmetric cubic two-degree-of-freedom systems with closed natural frequencies. Meccanica 38(3):335–348
22. Mojrzisch S, Twiefel J (2016) Phase-controlled frequency response measurement of a piezoelectric ring at high vibration amplitude. Arch Appl Mech 86(10):1763–1769
23. Monteil M, Thomas O, Touzé C (2015) Identification of mode couplings in nonlinear vibrations of the steelpan. Appl Acoust 89:1–15
24. Monteil M, Touzé C, Thomas O, Benacchio S (2014) Nonlinear forced vibrations of thin structures with tuned eigenfrequencies: the cases of 1:2:4 and 1:2:2 internal resonances. Nonlinear Dyn 75(1):175–200
25. Nayfeh AH (2000) Nonlinear interactions: analytical, computational and experimental methods. Wiley, New-York
26. Nayfeh AH, Lacarbonara W, Chin CM (1999) Nonlinear normal modes of buckled beams: three-to-one and one-to-one internal resonances. Nonlinear Dyn 18(3):253–273
27. Nayfeh AH, Mook DT (1979) Nonlinear oscillations. Wiley, New-York

28. Noël JP, Kerschen G (2017) Nonlinear system identification in structural dynamics: 10 more years of progress. Mech SystSignal Process 83:2–35
29. Noël JP, Schoukens M (2019) Cross-fertilising research in nonlinear system identification between the mechanical, control and machine learning fields: editorial statement. Mech Syst Signal Process 130:213–220
30. Peeters M, Kerschen G, Golinval JC (2011) Dynamic testing of nonlinear vibrating structures using nonlinear normal modes. J Sound Vib 330:486–509
31. Poincaré H (1892) Les méthodes nouvelles de la mécanique céleste. Gauthiers-Villars, Paris
32. Raman A, Mote CD Jr (2001) Effects of imperfection on the non-linear oscillations of circular plates spinning near critical speed. Int J Non-linear Mech 36:261–289
33. Renson L, Gonzalez-Buelga A, Barton DAW, Neild SA (2016) Robust identification of backbone curves using control-based continuation. J Sound Vib 367:145–158
34. Rosenberg RM (1966) On non-linear vibrations of systems with many degrees of freedom. Adv Appl Mech 9:155–242
35. Shaw S, Pierre C (1991) Nonlinear normal modes and invariant manifolds. J Sound Vib 150(1):170–173
36. Sieber J, Krauskopf B (2008) Control based bifurcation analysis for experiments. Nonlinear Dyn 51(3):365–377
37. Tan JJ, Touzé C, Cotté B (2015) Double polarisation in nonlinear vibrating piano strings. In: Proceedings of the third Vienna Talk on music acoustics. Vienna, Austria, pp 182–187
38. Thomas O, Lazarus A, Touzé C (2010) A harmonic-based method for computing the stability of periodic oscillations of nonlinear structural systems. In: ASME/IDETC 2010 International Design Engineering Technical Conference, Montreal, Québec, Canada
39. Thomas O, Touzé C, Chaigne A (2003) Asymmetric nonlinear forced vibrations of free-edge circular plates, part 2: experiments. J Sound Vib 265(5):1075–1101
40. Thomas O, Touzé C, Chaigne A (2005) Non-linear vibrations of free-edge thin spherical shells: modal interaction rules and 1:1:2 internal resonance. Int J Solids Struct 42(11):3339–3373
41. Thomas O, Touzé C, Luminais E (2007) Non-linear vibrations of free-edge thin spherical shells: experiments on a 1:1:2 internal resonance. Nonlinear Dyn 49(1–2):259–284
42. Tien WM, Namachchivaya NS, Bajaj AK (1994) Non-linear dynamics of a shallow arch under periodic excitation, I: 1:2 internal resonance. Int J Non-linear Mech 29(3):349–366
43. Touzé C (2014) Modal Analysis of nonlinear Mechanical Systems, chapter Normal form theory and nonlinear normal modes: theoretical settings and applications. Springer Series CISM courses and lectures, vol. 555, ISBN 978-3-7091-1790-2
44. Touzé C, Amabili M (2006) Non-linear normal modes for damped geometrically non-linear systems: application to reduced-order modeling of harmonically forced structures. J Sound Vib 298(4–5):958–981
45. Touzé C, Thomas O, Chaigne A (2002) Asymmetric nonlinear forced vibrations of free-edge circular plates. part 1: theory. J Sound Vib 258(4):649–676
46. Touzé C, Thomas O, Chaigne A (2004) Hardening/softening behaviour in non-linear oscillations of structural systems using non-linear normal modes. J Sound Vib 273(1–2):77–101
47. Williams CJH, Tobias SA (1963) Forced undamped nonlinear vibrations of imperfect circular disks. J Mech Eng Sci 5:325–335
48. Yasuda K, Asano T (1986) Nonlinear foced oscillations of a rectangular membrane with degenerated modes. Bull JSME 29(255):3090–3095